UNIVERSIDADE ESTADUAL PAULISTA “Júlio de Mesquita Filho”
FACULDADE DE CIÊNCIAS E TECNOLOGIA
Campus de Presidente Prudente
PPGCC – Programa de Pós-Graduação em Ciências Cartográficas

Retrieval of euphotic zone and Secchi disk depth in Bariri reservoir using OLI/Landsat-8 data

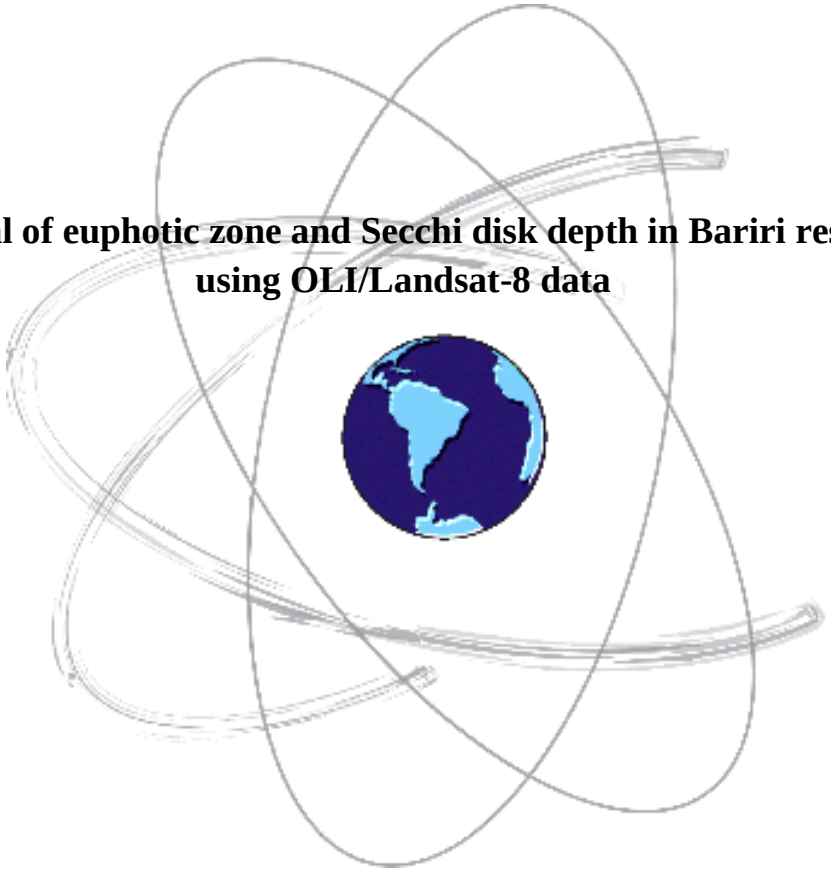

PRESIDENTE PRUDENTE

2018

Ana Carolina Campos Gomes

Retrieval of euphotic zone and Secchi disk depth in Bariri reservoir using OLI/Landsat-8 data

Dissertation presented to the Department of Cartography of the Faculty of Science and Technology of São Paulo State University "Júlio de Mesquita Filho" as part of the requirements for obtaining the Master degree in Cartographic Sciences.

Advisor: Prof. Dr. Enner Alcântara
Co-advisor: Dra. Thanan Walesza Pequeno Rodrigues

Presidente Prudente

2018

FICHA CATALOGRÁFICA

Gomes, Ana Carolina Campos.
G612r Retrieval of euphotic zone and Secchi disk depth in Bariri reservoir using OLI/Landsat-8 data / Ana Carolina Campos Gomes. – Presidente Prudente. -2018
78 f. : il.

Orientador: Enner Herenio de Alcântara
Coorientadora: Thanan Walesza Pequeno Rodrigues
Dissertação (mestrado) - Universidade Estadual Paulista. Faculdade de Ciências e Tecnologia, Presidente Prudente, 2018.
Inclui bibliografia

1. Atenuação da luz. 2. Qualidade da água. 3. Dados de satélite. 4. Modelos bio-ópticos. I. Gomes, Ana Carolina Campos. II. Alcântara, Enner Herenio de. III. Rodrigues, Thanan Walesza Pequeno. IV. Universidade Estadual Paulista. Faculdade de Ciências e Tecnologia. V. Título.

unesp

UNIVERSIDADE ESTADUAL PAULISTA

Câmpus de Presidente Prudente

CERTIFICADO DE APROVAÇÃO

TÍTULO DA DISSERTAÇÃO: RETRIEVAL OF EUPHOTIC ZONE AND SECCHI DISK DEPTH IN BARIRI RESERVOIR USING OLI/LANDSAT-8 DATA

AUTORA: ANA CAROLINA CAMPOS GOMES
ORIENTADOR: ENNER HERENIO DE ALCÂNTARA
COORIENTADORA: THANAN WALESZA PEQUENO RODRIGUES GUIMARÃES

Aprovada como parte das exigências para obtenção do Título de Mestra em CIÊNCIAS CARTOGRÁFICAS, área: AQUISIÇÃO, ANÁLISE E REPRESENTAÇÃO DE INFORMAÇOES ESPACIAIS pela Comissão Examinadora:

Prof. Dr. ENNER HERÊNIO DE ALCÂNTARA
Departamento de Engenharia Ambiental / Instituto de Ciência e Tecnologia de São José dos Campos

Prof. Dr. NILTON NOBUHIRO IMAI
Departamento de Cartografia / Faculdade de Ciencias e Tecnologia de Presidente Prudente

Dr. MILTON KAMPEL
Divisão de Sensoriamento Remoto / Instituto Nacional de Pesquisas Espaciais

Presidente Prudente, 23 de março de 2018

AGRADECIMENTOS

Meu primeiro agradecimento é a Deus, por todas as oportunidades concedidas e por ser luz e esperança em momentos árduos.

Agradeço imensamente aos meus pais, Marlene e Luís Antonio, que sempre estiveram presentes em minhas decisões, sendo meus apoios constantes, garantindo um lar cheio de amor e carinho. À minha irmã, Ana Laura, pela amizade, companheirismo e amor. Ao André, pela paciência e companheirismo.

Agradeço à orientação do Prof. Dr. Enner, por todo o comprometimento e competência dedicados ao desenvolvimento deste trabalho. Pelo incentivo na escrita de artigos e por proporcionar meu crescimento na pesquisa. À Dra. Thanan Rodrigues, pela coorientação, contribuindo com a evolução do trabalho.

Agradeço aos meus tios, primos e amigas de infância pelas conversas, apoios, orações e pela torcida em todos os momentos da minha vida.

Agradeço aos meus amigos do grupo de pesquisa SERTIE, em especial, ao grupo de pesquisa de Sensoriamento Remoto em sistemas aquáticos por me acolherem tão bem no grupo e no ambiente da Pós-Graduação, em especial agradeço:

À Nariane, Alisson, Fernanda e Luiz por toda atenção, contribuição; pela disponibilidade, disposição, confiança nas atividades do grupo e por toda a organização dos trabalhos de campo que possibilitaram as coletas dos dados usados neste trabalho. Agradeço ao Dr. Luiz e a Prof. Dra. Fernanda pela composição da banca no Exame de Qualificação do Mestrado.

À Sarah, Carol Ambrósio, Carol Piffer e Bruno Frias (GeoGrupo), pelo companheirismo e parceria, tornando as longas horas de aulas e estudos mais divertidas e menos árduas e pela amizade, que ainda permanece com a distância. Agradeço também a Nariane e ao Alisson, pela grande ajuda com o processamento dos dados, pela companhia nas horas de trabalho e nos intervalos e pelos laços criados, que culminaram em um convite muito especial.

Agradeço aos amigos da Pós-Graduação: Francielle, Guilherme, Tobias, Luiz Eduardo e Gabriel pelas conversas e cafés compartilhados, pelo acolhimento, ajuda e amizade.

Agradeço a toda infraestrutura fornecida pelo Programa de Pós-Graduação em Ciências Cartográficas (PPGCC), às funcionárias, Cida e Zilda, e a todos os professores que enriqueceram minha caminhada. À estrutura da FCT/UNESP, a todos os funcionários da unidade e aos professores da Graduação em Engenharia Ambiental, em especial a Profa. Dra. Maria Cristina Rizk.

Agradeço ao Prof. Dr. Nilton Imai pelo laboratório TIE e sua infraestrutura para a realização das análises dos dados. Ao Prof. Dr. Paulo César Rocha pela autorização do uso do Laboratório de Geologia, Geomorfologia e Recursos Hídricos. Ao Prof. Dr. Edivaldo Velini e aos técnicos da UNESP de Botucatu, pela permissão do uso dos equipamentos para análises laboratoriais.

Agradeço ao Conselho Nacional de Desenvolvimento Tecnológico e Científico - CNPq por conceder a bolsa de mestrado (Processo N.° 131737/2016-3) e pelo financiamento de projetos (Processos 400881/2013-6 e 472131/2012-5) e à Fundação de Pesquisa do Estado de São Paulo - FAPESP (Projetos 2012/19821-1 e 2015/21586-9) pelo financiamento dos trabalhos de campo.

A todas as pessoas envolvidas nesses dois anos de trabalho, meus sinceros agradecimentos!

RESUMO

O presente trabalho teve como objetivo estimar as profundidades da zona eufótica (Z_{eu}) e do disco de Secchi (Z_{SD}) a partir do coeficiente de atenuação da luz (k_d) utilizando dados do sensor *Operational Land Imager* (OLI)/Landsat-8 no reservatório de Bariri. Como importantes parâmetros de medida da claridade da água, k_d, Z_{eu} e Z_{SD} são afetados pelas substâncias opticamente significativas (SOS). A caracterização óptica do reservatório foi realizada a partir de duas campanhas de campo realizadas no período seco, aqui nomeadas como BAR1 (agosto/2016) e BAR2 (junho/2017), que contaram com análises das propriedades ópticas inerentes (POIs), das SOS e da coleta de dados radiométricos para o cálculo da reflectância de sensoriamento remoto (R_{sr}). A localização do reservatório de Bariri como o segundo do Sistema de Reservatórios em Cascata (SRC) do Rio Tietê promove a heterogeneidade dos seus níveis de eutrofização na direção montante-jusante além de caracterizá-lo como altamente produtivo. As campanhas de campo foram marcadas por uma significativa diferença nos valores de concentração de clorofila-*a* ([Chl-*a*]) que apresentou variação média entre 7,99 e 119,76 $\mu g\ L^{-1}$ com os maiores valores em BAR1, com decréscimo das SOS em BAR2 em relação a BAR1 e predomínio de material particulado orgânico (MPO) nas duas campanhas de campo; a turbidez variou entre 5,72 e 16,60 NTU. A absorção por matéria orgânica colorida dissolvida (a_{CDOM}) foi predominante nas duas campanhas de campo, sendo mais expressiva em BAR2. Para as estimativas de k_d, nove modelos empíricos e três modelos semi-analíticos baseados em dados radiométricos como razões entre as bandas azul/verde e azul/vermelho do sensor OLI/Landsat-8 e baseados em [Chl-*a*] foram avaliados. Considerando a propriedade óptica aparente (POA) do k_d, um modelo semi-analítico baseado em POIs e na distribuição angular da luz apresentou os menores erros (erro médio percentual absoluto – MAPE) de $\sim$ 40% em relação aos modelos empíricos de [Chl-*a*] com $\sim$ 60% e de $>$ 80% para os modelos empíricos baseados em razões de bandas. A partir das estimativas de k_d, modelos de estimativa de Z_{eu} e Z_{SD} foram avaliados. Para as estimativas de Z_{eu}, cinco modelos empíricos, baseados na relação entre o coeficiente de atenuação da luz da radiação fotossinteticamente ativa [k_d(PAR)] e de k_d em 490 nm [k_d(490)], e um modelo semi-analítico, baseado na equação de transferência radiativa, foram considerados; para as estimativas de Z_{SD}, um modelo semi-analítico foi testado. Os resultados obtidos foram melhores para um modelo empírico (erro percentual absoluto – ε) de Z_{eu} com $\sim$ 16% em relação ao modelo semi-analítico ($\varepsilon \sim 30\%$) e os erros nas estimativas de Z_{SD} foram de $\sim$ 57%. Os erros nas estimativas de k_d revelaram que a acurácia dos modelos empíricos foi comprometida devido à influência por CDOM e que o modelo semi-analítico, por considerar a natureza óptica de k_d como uma POA, apresentou os melhores resultados. As estimativas de Z_{SD} também foram afetadas pelas características ópticas de Bariri, não apresentando correlação com a matéria orgânica em BAR2, marcado pelo decréscimo de [Chl-*a*] e aumento dos valores de a_{CDOM}. Z_{eu} mostrou melhores resultados a partir de um modelo empírico calibrado com dados ópticos semelhantes aos do reservatório de Bariri em comparação ao modelo semi-analítico, desenvolvido para abranger as variações bio-ópticas sazonais e regionais. k_d, Z_{eu} e Z_{SD} foram espacializados a partir de imagens do sensor OLI/Landsat-8 permitindo a avaliação espaço-temporal desses parâmetros que apresentaram um padrão sazonal quando analisados em relação aos dados de precipitação. k_d apresentou variação entre 0,89 e 5,60 m^{-1} para o período analisado (2016) e Z_{eu} e Z_{SD} apresentaram variação entre 0,30 e 7,60 m e entre 0,32 e 2,95 m, respectivamente, para o período de 2014-2016. Pode-se concluir então, que apesar das estimativas de k_d, Z_{eu} e Z_{SD} terem sido afetadas pela influência de CDOM no reservatório de Bariri, o esquema semi-analítico foi capaz de estimar k_d com menor erro e permitiu as estimativas de Z_{eu} e Z_{SD}.

Palavras-chave: atenuação da luz; qualidade da água; dados de satélite; modelos bio-ópticos.

ABSTRACT

The objective of this present work was estimate the euphotic zone (Z_{eu}) and Secchi disk (Z_{SD}) depths from the light attenuation coefficient (k_d) using the Operational Land Imager (OLI)/Landsat-8 data in Bariri reservoir. The k_d, Z_{eu} and Z_{SD} are important water clarity parameters and are influenced by the optically significant substances (OSS). The optical characterization was carried out with data collected in two field campaigns in the dry period, here called BAR1 (august/2016) and BAR2 (june/2017), that included analysis of the inherent optical properties (IOPs), of the OSS and radiometric data to calculate the remote sensing reflectance (R_{rs}). The location of Bariri reservoir as the second of the Cascading Reservoir System (CRS) of Tietê River promotes the heterogeneity of the eutrophication levels from upstream to downstream besides characterizes the reservoir as highly productive. The field campaigns presented a significant difference in chlorophyll-*a* concentrations ([Chl-a]) with mean variation between 7.99 and 119.76 μg L^{-1} with the highest values in BAR1, with reduce of the OSS in BAR2 in relation to BAR1 and predominance of organic particulate matter (OPM) in both field campaigns and variation in turbidity from 5.72 to 16.60 NTU. The absorption of chromophoric dissolved organic matter (CDOM) was dominant in both field campaigns and more expressive in BAR2. For the k_d estimates, nine empirical models and three semi-analytical models based on radiometric data such as ratios of blue-green and blue-red bands of (OLI)/Landsat 8 sensor and based on [Chl-*a*] were evaluated. Considering the apparent optical property (AOP) of k_d, a semi-analytical model based on IOPs and the light angular distribution presented the lowest errors (mean absolute percentage error – MAPE) of ~ 40% in relation to the empirical models of [Chl-*a*] with ~ 60% and of > 80% for the empirical models based on the band ratios. Through the k_d estimates, models to derive Z_{eu} and Z_{SD} were evaluated. For the Z_{eu} estimates, five empirical models were considered based on the relation between the attenuation coefficient of the photosynthetically active radiation [k_d(PAR)] and the k_d at 490 nm [k_d(490)], and one semi-analytical model, based on the radiative transfer equation; for the Z_{SD} estimates, one semi-analytical model was tested. The empirical model of Z_{eu} showed the better results with the (unbiased absolute percentage error – ε) ~ 16% in relation to the semi-analytical model (ε ~ 30%) and the estimates errors of Z_{SD} were ~ 57%. The errors in k_d estimates revealed that the accuracy of the empirical models was affected by the CDOM influence in Bariri reservoir and the semi-analytical model presented a better performance when considering the optical nature of k_d as an AOP. The Z_{SD} estimates were also affected by the optical characteristics of Bariri with no correlation to the SPM in BAR2, where the [Chl-*a*] decreased and the a_{CDOM} increased. Z_{eu} showed better results from an empirical model calibrated with similar optical data to Bariri reservoir in relation to the semi-analytical model developed to be applied in a wide range of bio-optical seasonal and regional variations. The k_d, Z_{eu} and Z_{SD} were spatially distributed through OLI/Landsat-8 images allowing the temporal-spatial assessment of theses parameters, which presented a seasonal pattern when analyzed in relation to rainfall data. k_d presented variation from 0.89 to 5.60 m^{-1} to the analyzed period (2016) and Z_{eu} and Z_{SD} presented variations between 0.30 and 7.60 m and between 0.32 and 2.95 m, respectively, for 2014-2016 period. It can be concluded, therefore, that despite of the CDOM have affected the k_d, Z_{eu} and Z_{SD} retrievals in Bariri reservoir, the semi-analytical scheme was able to estimate k_d with lowest error and enable the Z_{eu} and Z_{SD} estimates.

Key-words: light attenuation; water quality; satellite data; bio-optical models.

LIST OF FIGURES

LIST OF TABLES

LIST OF ABREVIATIONS AND ACRONYMS

a	Absorption coefficient
a_p	Absorption Coefficient of Total Particulate
a_{NAP}	Absorption Coefficient of Non-Algal Particle
a_{CDOM}	Absorption Coefficient of Chromophoric Dissolved Organic Matter
a_{phy}	Absorption Coefficient of Phytoplankton
b_b	Backscattering coefficient
ρ	Effective Surface Reflectance
E_{sky}	Sky Irradiance
E_d	Downwelling Irradiance
E_d^+	Downwelling Irradiance at Water Surface
E_d^-	Downwelling Irradiance at Water Subsurface
E_d'	Normalized Downwelling Irradiance
ε	Unbiased Absolute Percentage Error
F	Fresnel Reflectance
F_r	Spectral Response Function
F_0	Extraterrestrial Solar Irradiance
$k_d(490)$	Attenuation Coefficient at 490 nm
$k_d(PAR)$	Attenuation Coefficient of the Photosynthetically Active Radiation
L_{sky}	Sky Radiance
L_t	Total Radiance
L_{SR}	Surface-Reflected Radiance
nL_w	Water-Leaving Radiance
Rrs	Remote Sensing Reflectance
R_{rs}^c	Remote-Sensing Reflectance Simulated
R	Irradiance Reflectance Beneath the Water Surface
R^2	Coefficient of Determination
S_{rs}	Sky Remote Sensing Reflectance
T_{rs}	Total Remote Sensing Reflectance
Z_{eu}	Euphotic Zone Depth
Z_{SD}	Secchi Disk Depth
APHA	American Public Health Association Protocol
AOP	Apparent Optical Property
CDOM	Chromophoric Dissolved Organic Matter
Chl-*a*	Chlorophyll-*a*
CRCC	Cascading Reservoir Continuum Concept
CRS	Cascading Reservoir System
CV	Coefficient of Variation
IOP	Inherent Optical Property
IPM	Inorganic Particulate Matter
LaSRC	Landsat Surface Reflectance Code
MAPE	Mean Absolute Percentage Error
MODIS	Moderate Resolution Imaging Spectroradiometer
NAP	Non-Algal Particle
OPM	Organic Particulate Matter
OSS	Optical Significant Substance
OLI/Landsat-8	Operand Land Imager onboard the Landsat-8 Satellite
PAR	Photosynthetically Active Radiation

PCA	Principal Component Analysis
QAA	Quasi-Analytical Algorithm
RMSE	Root Mean Square Error
RMSD	Root Mean Square Difference
SeaWiFS	Sea-viewing Wide Field-of-View Sensor
6SV	Second Simulation of the Satellite Signal in the Solar Spectrum Vectorial
SD	Standard Deviation
SPM	Suspended Particulate Matter
USGS	United States Geological Survey

CONTENTS

CHAPTER 1: Introduction

1.1 Background

Inland waters embrace the reservoirs, lakes and rivers and provide important support to diverse ecosystems and habitats. The reservoirs are commonly found in the Brazilian hydropower context and are subject of anthropogenic interferences as agricultural productions, grazing lands, urban centers and waste water which alter the natural biogeochemical characteristics of the water body. The reservoirs become environments where the algal proliferation and eutrophication processes are favorable by the nutrient increments through runoff and the increase of retention time, reducing the water quality (Lira *et al.*, 2009; Calijuri *et al.*, 2002).

The water quality is affected by the alteration of the quantities of the optical significant substances (OSS) such as the non-algal particles (NAP), phytoplankton and chromophoric dissolved organic matter (CDOM). The increase of OSS alters the turbidity and reduces the water clarity; the changes in turbidity affect the zooplankton community, increase the water temperature due to the high absorption of the sunlight by the suspended particles and reduce the dissolved oxygen rates in water column (Alcântara *et al.*, 2010).

The complex environment of the reservoir requires a qualitative and quantitative monitoring. The remote sensing based on satellite data allows the spatial-temporal study of a wide region in comparison with the traditional methods as point stations of sampling collection. Recent researches have shown suitable results in estimate water properties and constituents through remote sensing data in turbid inland waters (Yang *et al.*, 2013; Mishra *et al.*, 2014; Watanabe *et al.*, 2015; Alcântara *et al.*, 2016; Bernardo *et al.*, 2016; Rotta *et al.*, 2016; Zheng *et al.*, 2016; Rodrigues *et al.*, 2017).

An important study of water clarity monitoring was developed in Minnesota lakes using a 20 years of satellite data from Thematic Mapper (TM) and Enhanced Thematic Mapper Plus (ETM+) sensors (TM/Landsat 5 and ETM+/Landsat 7 series, respectively) generating satisfactory results in relation to *in situ* data and revealing the potentiality of the Landsat for optical complex waters (Olmanson *et al.*, 2008). The potentially of the Landsat systems for water clarity and CDOM measurements were evaluated in inland waters optically complex and CDOM-dominated. The OLI/Landsat-8 and ETM+/

Landsat-7 presented satisfactory results (coefficient of determination – R^2) for CDOM measures ($R^2 = 0.81$ and $R^2 = 0.79$, respectively) and for water clarity as the Secchi disk depth - Z_{SD} ($R^2 = 0.818$), relating the slight better performance of OLI/Landsat-8 to the higher radiometric sensitivity (Olmanson *et al.*, 2016). The OLI/Landsat-8 data presented a satisfactory performance ($R^2 = 0.82$) in k_d retrieval in extremely turbid inland lakes (Zheng *et al.*, 2016) and in k_d (mean absolute percentage error – MAPE = 10.35%) and Z_{SD} (linear correlation – R = 0.73) retrievals in optically variant inland waters producing good outcomes to spatial modeling of water transparency (Rodrigues *et al.*, 2017). The Operational Land Imager (OLI) data collected by the Landsat-8 satellite present a high spatial resolution of 30 meters and a swath width of 185 kilometers with increase of the signal-to-noise ratio (SNR) indicating that the Landsat-8/OLI is suitable to monitoring water-quality parameters in a regional scale (Zheng *et al.*, 2016).

The water clarity can be quantified from the vertical diffuse attenuation coefficient (k_d) which is estimated by measuring the decrease of downwelling irradiance with depth. The k_d is an intermediary product to estimate other two water clarity parameters: the euphotic zone (Z_{eu}) and the Secchi disk (Z_{SD}) depths. The Secchi disk is a black-and-white disk and the oldest instrument used to measure the water clarity (Lee *et al.*, 2015). The k_d is controlled by the inherent optical properties (IOPs) of water such as absorption (a) and scattering (b_b) processes and the angular distribution of light; the k_d at the wavelength of 490 nm is commonly derived from spectral remote sensing reflectance (Austin and Petzold, 1981; Mueller, 2000; Lee *et al.*, 2013) and is considered as the inverse of Z_{SD} which can be derived through satellite data in a semi-analytical model (Lee *et al.*, 2015; Lee *et al.*, 2016). The Z_{eu} corresponds to the depth where the downwelling irradiance achieves 1% of that measure at the water subsurface (Kirk, 1994). Considering the homogeneity of water column, a relation between k_d(PAR), the k_d at the photosynthetically active radiation (PAR), is used to estimate Z_{eu} in empirical and semi-analytical ways (Lee *et al.*, 2007; Zhao *et al.*, 2013; Liu *et al.*, 2016).

Lee *et al.* (2013) proposed a semi-analytical equation to derive k_d as the inversion of the IOPs estimated via a quasi-analytical algorithm (QAA) using the fifth version (QAA_v5). Yang *et al.* (2014) and Rodrigues *et al.* (2017) applied the semi-analytical equation and found that the lowest accuracy of k_d estimation and, consequently, the Z_{SD}

and Z_{eu} estimations, in turbid inland waters can be related to the propagated errors of the IOPs estimations.

The QAA is a multi-band effective algorithm with easily applicable sequential steps to estimate IOPs via remote sensing reflectance (R_{rs}) data for optically deep waters (Lee *et al.*, 2002). The sequence consists, firstly, in the conversion of R_{rs} into the subsurface reflectance (r_{rs}) and is followed by empirical, analytical and semi-analytical steps in four levels to acquisition of $a(\lambda)$ and particle backscattering coefficient ($b_{bp}(\lambda)$) and able to separate the $a(\lambda)$ in absorption coefficients of phytoplankton and CDOM (a_{φ} and $a_{CDOM,}$ respectively), allowing the estimations of Chl-*a* and CDOM concentrations. The empirical steps such as the estimation of *a* and b_{bp} were calibrated to seawater properties limiting the application of the QAA in optically complex waters (Yang *et al.*, 2013). Versions of QAA were created since the original version with modifications in the empirical steps and reference wavelengths (λ_0) in order to improve the results. The fifth version (QAA_v5), set for λ_0 = 560 nm, was applied in turbid inland waters, making possible the estimations of IOPs through adjustments in the algorithm (Le *et al.*, 2009; Yang *et al.*, 2013; Li *et al.*, 2016).

This work was carried out in Bariri reservoir, part of the Cascading Reservoir System (CRS) of Tietê River, São Paulo. Bariri is dominated by CDOM which compromise the phytoplankton activity, ecosystem productivity and present other effects on aquatic ecology and water chemistry that affect the water quality for human use (Zhang *et al.*, 2009; Brezonik *et al.*, 2015). The CDOM-rich freshwaters are greatly influenced by allochthonous source, susceptible to environmental factors such as hydrodynamic and anthropogenic activities (Zhu *et al.*, 2014) that can compromise the k_d, Z_{eu} and Z_{SD} estimations.

1.2. Hypothesis

Considering the nature of k_d, the semi-analytical algorithm developed by Lee *et al.* (2013) respects the dependence on the IOPs and the angular distribution light and, therefore, will be able to produce good results in inland waters through the original form of QAA_v5, set for the Landsat-8/OLI center bands, in relation to others semi-analytical and empirical models analyzed in this study. Thus, our hypothesis bases on the fact that the semi-analytical algorithm used to derive k_d, even with errors related to the

estimative of the IOPs via QAA_v5 when applied to turbid inland waters, will enable the estimation of Z_{eu} and Z_{SD} through a semi-analytical scheme.

1.3. Objectives

This study aimed to investigate the performance of a semi-analytical scheme to estimate Z_{eu} and Z_{SD} using k_d estimates from remotely sensed data in Bariri reservoir. For this, the specific objectives were to:

- Characterize the optical properties of Bariri reservoir;
- Evaluate the performance of nine empirical and three semi-analytical models of k_d to choose the more suitable one for Bariri reservoir;
- Evaluate the performance of six Z_{eu} algorithms and one semi-analytical model of Z_{SD} using as input the k_d model best fitted for the Bariri reservoir and choose the best models to map the Z_{eu} and Z_{SD} in Bariri reservoir;
- Assess the temporal-spatial distribution of derived k_d, Z_{eu} and Z_{SD};
- Assess the effects of CDOM and the seasonality in rainfall terms on the performance of the water clarity parameters.

1.4. Outline of the Dissertation

This dissertation is organized in 4 chapters. The chapter 1 introduces the theme, delineating the problems of this research and the steps followed to answer the questions proposed. The chapter 2 corresponds to the investigation of the performance of k_d models in the aquatic environment of Bariri reservoir, exploring the limiting factors of the CDOM dominance on the absorption coefficients in the evaluated models structure. The chapter 3 corresponds to the evaluation of models to retrieve Z_{eu} and Z_{SD} through the derived k_d data and their performances in the field campaigns. The relation of Z_{eu} and Z_{SD} with the water constituents also was evaluated. The chapters 2 and 3 present the characterization of the study site, the description of the field campaigns, sampling planning and the optical properties characterization of the study site. Lastly, the chapter 4 highlights the main findings and challenges of this research.

CHAPTER 2: Retrieval of diffuse attenuation coefficient in inland waters dominated by colored dissolved organic matter

2.1. Introduction

The diffuse attenuation coefficient (k_d) is an apparent optical property (AOP) and is defined as the exponential decrease of the ambient downwelling irradiance (E_d) with depth, therefore is related to light penetration and availability and can be used to predict the euphotic depth. AOP are those properties that depend both on the medium and on the geometric structure of the radiance distribution (Mobley, 1994).

k_d is largely determined by the inherent optical properties (IOPs), absorption (*a*) and backscattering (b_b) coefficients in first order and, in lesser magnitude dependent on the incident radiation field as the Sun angle. IOPs are properties of the medium and do not depend on the ambient light field (Mobley, 1994).

Non-algal particles (NAP), phytoplankton, chromophoric dissolved organic matter (CDOM) and water are considered the four optically significant substances (OSS) that control the k_d. The k_d at 490 nm [$k_d(490)$] is generally considered and classified as a parameter of water quality, therefore is essential for monitoring the eutrophication process due to light attenuation by phytoplankton growth or suspended matter (Zheng *et al.*, 2016). Since light availability is a critical regulator of physical, chemical and biological processes the accurate estimation of k_d is critical to better understanding and modeling primary productivity, heat and gas transfer in aquatic systems.

In order to estimate $k_d(490)$, some empirical algorithms were developed using a direct form from normalized water-leaving radiance (nL_w) or remote sensing reflectance (R_{rs}) ratios or indirect form through products based on chlorophyll-*a* concentrations ([Chl-*a*]) (Morel *et al.*, 2007; Mueller, 2000; Mueller and Tress, 1997; Chauhan *et al.*, 2003; Werdell, 2005; Kratzer *et al.*, 2008; Zhang and Fell, 2007; Wang *et al.*, 2009). However, these models are considered site specific, which is a limiting factor for a broader application. Wang *et al.* (2009) and Lee *et al.* (2013) came up with a semi-analytical approach covering a wide range of waters. Wang *et al.* (2009) used a combination of two models suitable for ocean and turbid coastal waters, aiming to improve the application range of $k_d(490)$ estimations. The model from Lee *et al.* (2013) considered the IOPs derived from R_{rs} through a quasi-analytical algorithm QAA (Lee *et al.*, 2002), and the solar zenith angle using the radiative transfer theory. The algorithm

make it possible the estimation of spectral k_d, as well as $k_d(490)$, for water bodies ranging from the clearest ocean to turbid coastal waters.

Even so, studies showing the use of remote sensing for $k_d(490)$ estimation in tropical productive inland waters are hampered by the lack of *in situ* data and theoretical framework to predict and interpret ocean color data in such waters (Gallegos *et al.*, 1990). The optically complexity of turbid waters (mineral suspended solids, algae and associated organic particles) produce multiple scattering making it difficult the mathematical analysis of radiative transfer (Gallegos *et al,*. 1990). From our understanding there are no investigation of $k_d(490)$ estimation in inland waters dominated by CDOM, which is an optically active component of dissolved organic matter and plays an important role in the cycling carbon.

CDOM is considered an important water quality indicator due to its impact on the drink water, carbon balance and aquatic ecosystems; mainly because CDOM affects penetration of photosynthetically active radiation into the water column, which affects the primary productivity. Most models use R_{rs} or nL_w from the blue-green spectral region, in which the CDOM has high absorption. Because of that the following questions came up: (1) The $k_d(490)$ models that use the blue/green ratio will be impacted in such way that the errors will make it impossible to use? (2) How will these models be impacted in the presence of high [Chl-*a*]? (3) Semi-analytical models, which use IOPs as input data will perform better than the empirical ones? (4) What are the perspectives for k_d monitoring from space in inland waters dominated by CDOM?

Therefore the main goal of this paper was to assess the performance of algorithms to estimate $k_d(490)$ in inland waters dominated by CDOM, which are widely available to end users. We tested nine empirical and three semi-analytical algorithms. The selected models will help us to answer the above questions.

2.2. Materials and Methods

2.2.1. Study Area and Sampling Planning

Bariri hydroelectric reservoir (22° 9’ 49.260” S 48° 44’ 21.420” W) is in the middle of the São Paulo State and is part of the Cascading Reservoir System (CRS) of the Tietê River (Figure 2.1). Bariri is the second of a total of six reservoirs and presented the smallest flooded area of 63 km² in an average altitude of 450 meters. The Bariri

reservoir is situated in a tropical climate with a dry period (April-September) and a wet period (October-March) according to Köppen classification. The water retention time varies among 7 and 24 days (Tundisi *et al.*, 2008).

Figure 2.1. Graphics showing the location of (a) São Paulo State in Brazilian context; (b) Bariri Reservoir in the Cascading Reservoir System of Tietê River; (c) sampling points of the two field campaigns carried out, BAR1 and BAR2 and (d) precipitation rate data (mm) from NASA's GIOVANNI database for the period of 2014-2017 (TRMM Data Product; Spatial Resolution of .0.25º; Monthly Temporal Resolution). In 2017, the precipitation monthly averages were available just until July month.

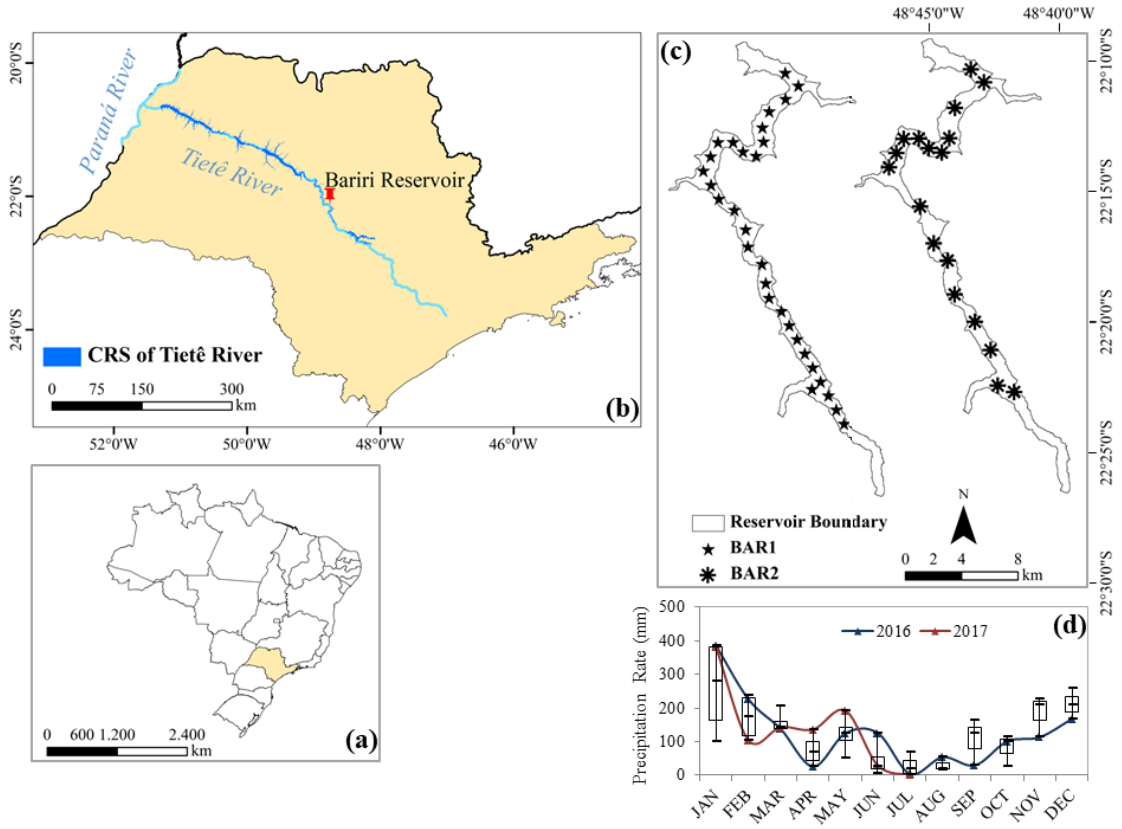

The amount of wastewater coming from the metropolitan region of Tietê River characterizes the Bariri Reservoir as highly productive water with high average concentrations of total nitrogen (2750 µg L^{-1}), phosphorus (87 µg L^{-1}) and [Chl-*a*] (55.8 µg L^{-1}) with the phytoplankton community dominated by cyanobacteria. As the second reservoir, the Cascading Reservoir Continuum Concept (CRCC) effect promotes the heterogeneity of the eutrophication levels in upstream to downstream in Bariri, revealed by the water transparency of the water (Barbosa *et al.*, 1999).

Two fieldworks were carried out where in the first one (BAR1), 30 samples were collected from 15 to 18 August 2016 and in the second one (BAR2), 18 samples were

taken from 23 to 24 June 2017 (see Figure 2.1 for samples locations). The days of the field campaigns were determined according to the temporal resolution of OLI/Landsat-8 aiming to match the data collection with the satellite overpass the study site.

2.2.2. Water quality and Optical Data

The wind speed (m s^{-1}), pH, depth (m), Secchi disk depth (Z_{SD}; m) and turbidity (NTU) were measured in the field with an anemometer, pHmeter, Secchi disk and turbidity meter, respectively. The water samples were collected in the field to derive the OSS, such as the Chl-*a* and the suspended particulate matter (SPM) as well as the inorganic (IPM) and organic particulate matter (OPM) concentrations according to Golterman *et al.* (1978) and the American Public Health Association Protocol (APHA, 1998), respectively.

The IOP data analysis followed the methodology proposed in Bricaud *et al.* (1981) for a_{CDOM} while for the absorption coefficients of non-algal particle (a_{NAP}) and the total particulate (a_p), that consists in the sum of a_{NAP} and a_φ, the acquisition and analyses were made in accordance with the Transmittance-Reflectance method according to Tassan and Ferrari (1995, 1998, 1999).

The radiometric data were obtained from the two hyperspectral RAMSES sensors (TriOS, Rastede, Germany). The sky and total radiance data (L_{sky} and L_t, respectively, both in W m^{-2} sr^{-1}) and the downwelling and sky irradiance data (E_d and E_{sky}, respectively, both in W m^{-2}) were taken with the sensors fixed by a steel frame in the boat, in a configuration of 40° from nadir (zenith) and to azimuthal angle of 90° in order to minimize the specular reflection (Mobley (1999). The radiometric quantities were used to calculate the remote sensing reflectance according to Equation (2.1).

$$R_{rs}(\lambda) = \frac{L_t(\lambda) - L_{SR}(\lambda)}{E_d + (\lambda)} = \frac{L_t(\lambda) - (\rho L_{sky}(\lambda))}{E_d + (\lambda)} \quad (2.1)$$

where E_d+ is the downwelling irradiance measured at the water surface. The L_{SR} is the surface-reflected radiance and consists in a multiplicative product of L_{sky} and ρ - an effective surface reflectance. The ρ value (≈0.02-0.05) depends on the viewing geometry and spectral variation. In agreement with that, Lee *et al.* (2010) proposed a calculation approach of R_{rs} as a function of the total remote-sensing reflectance (T_{rs},

ratio of L_t to E_d) and sky remote-sensing reflectance (S_{rs}, ratio of L_{sky} to E_d) for each L_t and L_{sky} scan from the Equation (2.2):

$$R_{rs}(\lambda) \approx T_{rs}(\lambda) - F \times S_{rs}(\lambda) - \Delta \quad (2.2)$$

where F refers to Fresnel reflectance and it was set as 0.021 according to the viewing geometry; Δ is a spectrally constant settled before R_{rs} can be derived (Lee *et al.*, 2010). In oceanic waters, the R_{rs} is negligible in the red and near-infrared wavelengths and Δ can be assumed as zero beyond 700 nm, however, for turbid inland waters, the IOPs have a significant influence in R_{rs}, thus, one alternative is to model the spectral R_{rs} based on the IOPs, and then resolve Δ after comparing modeled R_{rs} and derived R_{rs} from Equation (2.2).

In sequence, the R_{rs} used in estimates models of k_d must be simulated to the satellite signal at each spectral channel centered at a wavelength (λ = 443; 482; 561; 655 nm). The band simulation consists in the convolution of the radiation signal of hyperspectral sensor and the spectral response function [$F_r(\lambda)$] of the OLI sensor in wavelength interval of the spectral resolution (Barsi *et al.*, 2014):

$$R_{rs}^{c}(\lambda) = \frac{\int_{x_{min}}^{x_{max}} R_{rs}(\lambda) F_r(\lambda)}{\int_{x_{min}}^{x_{max}} F_r(\lambda)} \quad (2.3)$$

where $R_{rs}^{c}(\lambda)$ is the remote-sensing reflectance simulated at center wavelength; x_{max} and x_{min} are, respectively, the maximum and minimum values of the sensor spectral channel.

According to E_d data, the $k_d(490)$ in both field campaigns was determined as the slope of E_d at subsurface depth (z) [$E_d^-(z)$] (Mobley, 1994):

$$k_d(\lambda, z) = \frac{1}{E_d^-(\lambda)} \frac{dE_d^-(\lambda)}{dz} \quad (2.4)$$

In order to eliminate the noise in the $E_{sky}(\lambda)$ due to changes in the sun illumination condition caused by cloud cover during the $E_d^-(z)$ measurements, a normalization factor was required in all scans. The E_d normalization consists in a division of E_{sky} at first scan $t(z_1)$ to E_{sky} at subsequent scans $t(z_i)$ as factor normalization of the $E_d^- t(z_i)$ according Mishra *et al.* (2005) and Mueller (2000):

$$E'_d(z_i,\lambda) = \frac{E_d(z_i,\lambda)E_{sky}(t(z_1),\lambda)}{E_{sky}(t(z_i),\lambda)} \quad (2.5)$$

where $E'_d(z_i,\lambda)$ is the normalized $E_d^-t(z_i)$.

2.2.3. $K_d(490)$ models

The Table 2.1 summarizes the $k_d(490)$ algorithms tested in this study.

Table 2.1. $k_d(490)$ models developed for clear ocean, coastal, turbid ocean, slightly turbid and global waters.

Type	Model	Formula	Calibration Dataset
Empirical model with Chl-*a* concentration	Morel *et al.* (2007)	$k_d(490) = 0.0166 + 0.0773[Chla]^{0.6715}$ $k_d(490) = 0.0166 + 0.0724[Chla]^{0.6896}$	Clear Ocean Waters
Empirical model with normalized water-leaving radiance (nL_w) or remote sensing reflectance (R_{rs})	Mueller (2000)	$k_d(490) = 0.016 + 0.15645\left(\frac{nL_w(490)}{nL_w(555)}\right)^{-1.5401}$	
	Mueller and Tress (1997)	$k_d(490) = 0.022 + 0,1\left(\frac{nL_w(443)}{nL_w(555)}\right)^{-1.29966}$	Clear Ocean Waters
	Chauhan *et al.* (2003)	$k_d(490) = 0.022 + 0.124\left(\frac{nL_w(443)}{nL_w(555)}\right)^{-1.64}$	
	Werdell (2005)	$k_d(490) = 0.1853\left(\frac{nL_w(490)}{nL_w(555)}\right)^{-1.349}$	Global Waters
	Kratzer *et al.* (2008)	$k_d(490) = 0.022 + e^{-1.03\ln\frac{Rrs(490)}{Rrs(620)}-0.18}$	Coastal Waters
	Zhang and Fell (2007)*	$k_d(490) = 10^{0.094-1.302\log\frac{Rrs(490)}{Rrs(665)}+0.247\log\left(\frac{Rrs(490)}{Rrs(655)}\right)^2-0.021\log\left(\frac{Rrs(490)}{Rrs(655)}\right)^3} + k_w(490)$	Turbid Ocean Waters
	Wang *et al.* (2009)	$k_d(490) = -3.7591 + 4.7424\left(\frac{R_{rs}(655)}{R_{rs}(482)}\right)$	Slightly Turbid Waters
Semi-analytical model	Wang *et al.* (2009)	$k_d(490) = \frac{2.697x10^{-4}}{R(488)} + 1.045\frac{R(667)}{R(488)} + 4.18\left[7x10^{-4} + 2.7135R(667)\right]$ $x\left\{1 - 0.52exp\left[\frac{-2.553x10^{-3}}{R(488)} - 9.817\frac{R(667)}{R(488)}\right]\right\}$ $k_d(490) = \frac{-9.785x10^{-4}}{R(488)} + 0.8321\frac{R(645)}{R(488)} + 4.18\left[-2.54x10^{-3} + 2.1598R(645)\right]$ $x\left\{1 - 0.52exp\left[\frac{9.19x\,10^{-3}}{R(488)} - 7.81\frac{R(645)}{R(488)}\right]\right\}$	Slightly Turbid Coastal Waters
	Lee *et al.* (2013)	$k_d(\lambda) = (1 + 0.005 \times \theta_s)a(\lambda) + \left(1 - 0.265\frac{b_{bw}(\lambda)}{b_b(\lambda)}\right) \times 4.259 \times (1 - 0.52 \times e^{-10.8\times a(\lambda)})b_b(\lambda)$	Global Ocean Waters

*$k_w(490) = 0.016m^{-1}$ is a constant of the diffuse attenuation coefficient for pure sea water (Zhang and Fell, 2007).

We have tested three types of model: (1) empirical relationships between the k_d and [Chl-*a*]; (2) empirical relationship between the water-leaving radiance (nL_w) and k_d and (3) semi-analytical models which are based on radiative transfer models.

The nL_w is calculated trough the conversion of R_{rs} as $nL_w = F_0(\lambda)R_{rs}(\lambda)$ where $F_0(\lambda)$ is the extraterrestrial solar irradiance (Wang *et al.* 2009; Zhao *et al*., 2013). The $R(\lambda)$ is the irradiance reflectance beneath the water-surface and is calculated as a function of extraterrestrial solar irradiance [$F_0(\lambda)$] and nL_w (Wang et al., 2009).

The equations from Morel *et al.* (2007) are based on [Chl-*a*] whereas the others empirical algorithms use a simple ratio of $nL_w(\lambda)$. The Zhang and Fell (2007) and Wang *et al.* (2009) are the unique empirical models based on a $R_{rs}(\lambda)$ ratio. The semi-analytical model of Wang *et al.* (2009) was developed using the $R(\lambda)$ ratios and the Lee *et al.* (2013) model previously requires the calculation of $a(\lambda)$ and $b_b(\lambda)$ which are obtained from the QAA_v5 (the version 5 was used in this study) with R_{rs} as input at the reference wavelength (λ_0) of 561 nm, the nearest OLI center band of λ_0 = 55x of QAA_v5. In the equation, the zenith solar angle (θ_s) was set as 40º following the geometry used in the radiometric data collection.

2.2.4. OLI/Landsat-8 Data Processing and Acquisition

The Landsat 8 Surface Reflectance on-demand data generated by the Landsat Surface Reflectance Code (LaSRC) were obtained in the U.S. Geological Survey platform (*http://earthexplorer.usgs.gov/*). The LaSRC algorithm for atmospheric correction was developed using the Second Simulation of the Satellite Signal in the Solar Spectrum Vectorial (6SV) model. The algorithm uses the OLI Coastal Aerosol Band (0.433–0.450 μm) which works as cover for shorter wavelength as the blue band in previous Landsat and is helpful to retrieve aerosol properties (Vermote *et al*., 2016). Pahlevan *et al.* (2017) and Bernardo *et al.* (2016) showed that LaSRC is a consistent product to derive aquatic estimates. A total of 10 atmospherically corrected images (Path/Row 221/75) were acquired during the year of 2016, covering the months from February to November. The criteria used for the images choice was attributed to cloud free data over the reservoir.

To obtain the $nL_w(\lambda)$ and $R(\lambda)$ and to test the $k_d(490)$ models, the surface reflectance images were divided by π to convert them into R_{rs} (Moses *et al.*, 2012). The $k_d(490)$ model with the best performance was applied to the time-series of LaSRC

images selected to obtain the spatial distribution of the vertical attenuation coefficient. The $k_d(490)$ model best fitted for Bariri reservoir was validated through the use of the satellite image from August 15th 2016, correspondent to the first day of BAR1. In the same way, the LaSRC accuracy in $k_d(490)$ estimations was evaluated from the analysis between the R_{rs} converted images with the R_{rs} calculated from TriOS data in BAR1.

2.2.5. Statistical Analysis and Accuracy Assessment

Statistical analyses, including calculations of the maximum, minimum and average values and linear and non-linear regressions were performed. The $k_d(490)$ analyzed models were applied for BAR1 and BAR2 datasets. The Root Mean Square Error (RMSE), Mean Absolute Percentage Error (MAPE) and the *bias* were used to assess the accuracy of the $k_d(490)$ models.

$$\mathrm{RMSE} = \sqrt{\frac{1}{j}\sum_{i=1}^{j}\left(x_{est,i} - x_{mea,i}\right)^2} \quad (2.6)$$

$$\mathrm{MAPE} = \frac{100\%}{j}\sum_{i=1}^{j}\left|\frac{x_{est,i} - x_{mea,i}}{x_{mea,i}}\right| \quad (2.7)$$

$$bias = \frac{1}{j}\sum_{i=1}^{j}\left(x_{est,i} - x_{mea,i}\right) \quad (2.8)$$

where x_{est} is the $k_d(490)$ estimated value and x_{mea} is the *in situ* measure of $k_d(490)$.

2.3. Results and Discussion

2.3.1. Remote Sensing Reflectance Spectra

In BAR1 spectral curves (Figure 2.2) is possible to see a high absorption feature at about 680 nm and a reflectance peak at approximately 710 nm that can be associated with the Chl-*a* pigment. The sampling points with the highest [Chl-*a*] presented a significant peak at 550 nm, expected for water with a great amount of algae, just as seen in field campaign. The increase of reflectance in longer wavelength was an indicative of total suspended matter concentration increases. The [Chl-*a*] in BAR1 was approximately 37 times higher than in BAR2 dataset (see Table 2.2), which explains why the absorption by pigments was more evident during the first survey.

In all data set, the organic particles were predominant (Table 2.2), therefore the spectra of BAR1 and BAR2 were quite similar with lesser reflectance magnitude of BAR2 mainly because lowest OSS concentrations. In BAR2 spectra, the feature characteristic of phytoplankton absorption was not evident such as was for BAR1 due to the decrease of [Chl-*a*] in relation to BAR1, with the exception of the feature of the sampling point that presented the maximum value of [Chl-*a*] in BAR2 (19.11 µg L-1).

Figure 2.2. The R_{rs} spectra for BAR1 (a) and BAR2 (b) surveys.

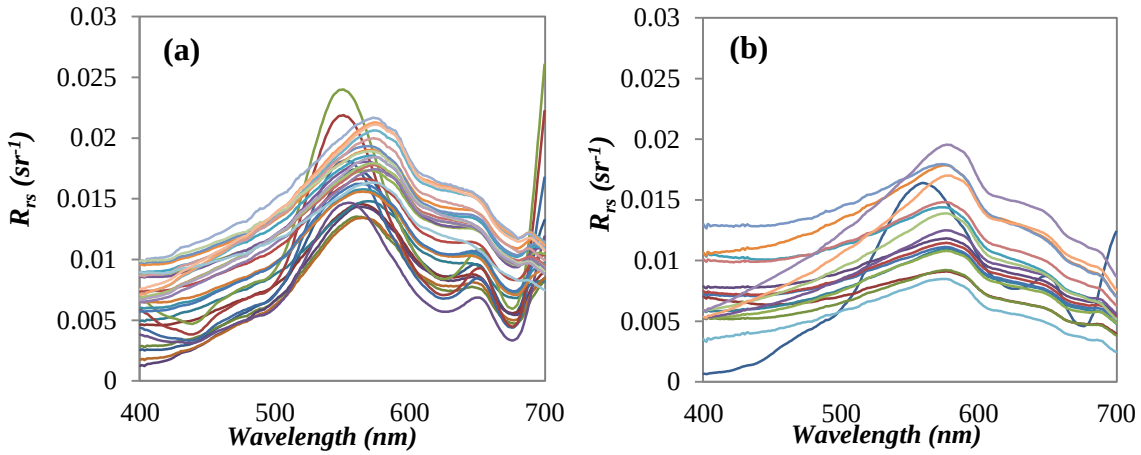

The light absorption by CDOM was the highest in both field campaigns (1.57 ± 0.37 m^{-1} in BAR1 and 1.98 ± 0.76 m^{-1} in BAR2) in relation to light absorption by others OSS. In CDOM-rich lakes, the spectra shapes vary according to CDOM levels and the influence of other substances in absorption processes (Brezonik *et al.*, 2015). In BAR1, the light absorption was dominated by CDOM, however the reflectance spectra assumed a shape of Chl-*a* due to the high concentrations and presented low reflectance values at 400-500 nm. In BAR2, with the predominance of CDOM absorption and reduction of OSS concentrations, the reflectance values assumed a nearly flat feature at ~ 600 nm.

2.3.2. Optical Properties and Water Constituents

Table 2.2 presents the descriptive statistics for optical and water parameters for the two field campaigns, BAR1 and BAR2. In BAR1, the sky was sunny in the most of the days with some moments of overcast. In BAR2, the sky was more favorable with sunny days during all field campaign. In all dataset, the average wind speed was 3.32 ± 1.77 m s^{-1} producing some small waves on the water surface. The minimum values for both

field campaigns were 0 m s^{-1} and the maximum value was 8 m s^{-1} for BAR1 and 6.50 m s^{-1} for BAR2.

Table 2.2. Descriptive statistics for optical and water quality parameters for BAR1, BAR2 and the mixed data.
S.D. = Standard Deviation. C.V. = coefficient of variation.

Field Campaigns	Parameters	Minimum	Maximum	Mean	S.D.	C.V.
BAR1 (N = 30)	**Z_{SD} (m)**	0.50	1.60	1.16	0.23	20.03%
	Turbidity (NTU)	7.80	80.90	16.60	7.61	45.82%
	pH	6.10	9.90	7.94	0.83	10.46%
	Wind Speed (m s^{-1})	0.00	8.00	3.47	1.80	51.73%
	k_d(482) (m^{-1})	1.87	3.98	2.80	0.30	10.69%
	[Chl-*a*] (µg L^{-1})	25.67	709.89	119.76	96.43	80.52%
	[SPM] (mg L^{-1})	3.60	40.33	8.40	4.64	55.25%
	[IPM] (mg L^{-1})	0.90	4.00	2.35	0.51	21.92%
	[OPM] (mg L^{-1})	1.40	36.33	6.06	4.57	75.43%
	a_{phy}(482) (m^{-1})	0.16	1.25	0.41	0.22	53.46%
	a_{NAP}(482) (m^{-1})	0.15	0.55	0.33	0.09	28.52%
	a_{CDOM}(482) (m^{-1})	0.92	2.74	1.57	0.37	23.73%
BAR2 (N = 18)	**Z_{SD} (m)**	1.60	2.50	2.06	0.19	9.31%
	Turbidity (NTU)	3.48	8.80	5.72	1.25	21.92%
	pH	6.83	7.28	6.97	0.13	1.89%
	Wind Speed (m s^{-1})	0.00	6.50	3.06	1.72	56.28%
	k_d(482) (m^{-1})	1.54	2.34	1.79	0.12	6.47%
	[Chl-*a*] (µg L^{-1})	3.82	19.11	7.99	3.27	40.90%
	[SPM] (mg L^{-1})	0.20	2.60	1.59	0.44	27.92%
	[IPM] (mg L^{-1})	0.24	1.30	0.58	0.24	42.39%
	[OPM] (mg L^{-1})	0.40	1.60	1.11	0.32	28.81%
	a_{phy}(482) (m^{-1})	0.02	0.11	0.07	0.02	26.67%
	a_{NAP}(482) (m^{-1})	0.06	0.19	0.12	0.03	26.39%
	a_{CDOM}(482) (m^{-1})	0.76	4.38	1.98	0.76	38.17%
All data (N = 48)	**Z_{SD} (m)**	0.50	2.50	1.49	0.43	29.03%
	Turbidity (NTU)	3.48	80.90	12.66	6.34	50.03%
	pH	6.10	9.90	7.58	0.71	9.39%
	Wind Speed (m s^{-1})	0.00	8.00	3.32	1.77	53.37%
	k_d(482) (m^{-1})	1.55	3.98	2.42	0.51	21.10%
	[Chl-*a*] (µg L^{-1})	3.82	709.89	77.84	77.15	99.10%
	[SPM] (mg L^{-1})	0.20	40.33	5.79	4.05	69.82%
	[IPM] (mg L^{-1})	0.20	4.00	1.96	0.79	40.25%
	[OPM] (mg L^{-1})	0.40	36.33	4.99	3.96	79.52%
	a_{phy}(482) (m^{-1})	0.02	1.25	0.28	0.19	67.72%
	a_{NAP}(482) (m^{-1})	0.06	0.55	0.25	0.12	45.70%
	a_{CDOM}(482) (m^{-1})	0.76	4.38	1.72	0.52	30.36%

The water collected in BAR1 was green in most of the samples, which is explained by the presence of phytoplankton pigments due to high [Chl-*a*] averaging 119.76 ± 96.43 µg L^{-1}, and ranging between 25.67 and 709.89 µg L^{-1}. In BAR2, the [Chl-*a*] variability reduced significantly with average of 7.99 ± 3.27 µg L^{-1}, varying from 3.82 to 19.11 µg L^{-1}. Therefore, the mixed data resulted in a range from 3.82 to 709.89 µg L^{-1} of [Chl-*a*].

The SPM concentration (average of 8.40 ± 4.64 mg L^{-1}) showed predominance of organic particles with average of 6.06 ± 4.57 mg L^{-1} in BAR1 as well as in BAR2, where the organic compounds predominated the SPM (1.59 ± 0.44 mg L^{-1}) with average of 1.11 ± 0.32 mg L^{-1}. The SPM presented low concentration in BAR2. In all dataset, the organic particle dominated the SPM concentration, with an average of 4.99 ± 3.96 mg L^{-1}. In respect to absorption, $a_{NAP}(482)$ was higher in BAR1 (average of 0.33 ± 0.09 m^{-1}) than BAR2 (average of 0.12 ± 0.03 m^{-1}). The $a_{CDOM}(482)$ averaged 1.57 ± 0.37 m^{-1} in BAR1 and 1.98 ± 0.76 m^{-1} in BAR2. The $a_{\varphi}(482)$ averaged 0.41 ± 0.22 m^{-1} in BAR1 and 0.07 ± 0.02 m^{-1} in BAR2.

The Figure 2.3 shows the average spectra of IOPs for BAR1 and BAR2 dataset.

Figure 2.3. Absorption spectra of NAP, phytoplankton, CDOM and pure water (a_w) in BAR1 (a) and BAR2 (b).

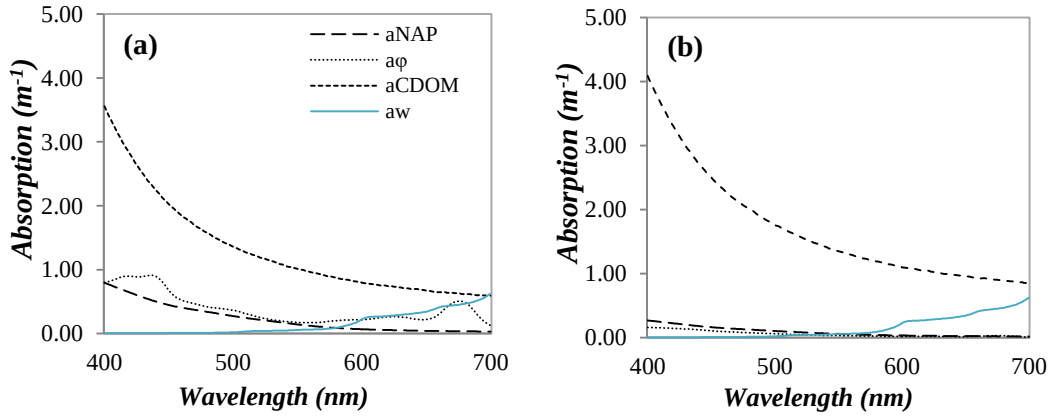

The a_{CDOM} spectra presented the highest values in all spectral range in both field campaigns. On the other hand, the a_{φ} spectra was higher for BAR1 than BAR2; it is possible to see two peaks of absorption at 450 and 670 nm in BAR1 whereas in BAR2, the characteristic a_{φ} spectra was not evident. In BAR2, the a_{φ} and a_{NAP} spectra were similar with light absorption by NAP slightly higher than the absorption by phytoplankton, with the absorption curve decay at 550 nm. The absorption curve of

NAP at blue portion of the visible spectrum represents the typical spectra of mineral and/or detrital particles, verified in BAR1 and BAR2 absorptions spectra. The atypical a_φ spectra in BAR2, with the exponentially increase at wavelengths shorter than 500 nm, indicate an environment with elevated CDOM absorption (Binding *et al.*, 2008).

Among the three absorption coefficients already mentioned, $a_{CDOM}(482)$ showed the highest values in both field campaigns. Zhang *et al.* (2009) proved that high [Chl-*a*] and high a_{CDOM} indicate that the accumulation and degradation of phytoplankton were a source of CDOM in eutrophic waters. It suggests that the organic matter is possibly originated by the phytoplankton degradation in BAR1. In BAR2, the a_{CDOM} is also predominant with significant reduction of [Chl-*a*] which can suggest an allochthonous source of CDOM. The Bariri reservoir has been undergoing impacts due to the sugarcane production and the input of urban and industrial wastewaters (Pamplin, 2004).

The proportional contribution of the IOPs in BAR1 and BAR2 among the total absorption (a_t) budget in Bariri aquatic environment was computed considering the OLI bands (443, 482, 561 and 655 nm) (Figure 2.4a-d). The light absorption in BAR1 was predominant by CDOM in all wavelengths, with 63.49% ± 11.59%; 67.74% ± 9.98% and 69.82% ± 12.56% at 443, 482 and 655 nm, respectively. At 561 nm, the CDOM contribution was the highest with 76.08% ± 8.84%. The same was verified for BAR2, where the CDOM predominance was even higher with 88.28% ± 5.43% at 443 nm; 88.85% ± 5.70% at 482 nm; 92.07% ± 5.24% at 561 nm but with the highest contribution at 655 nm with 94.02% ±.6.03%.

In BAR1, the phytoplankton contributed with 22.40% ± 13.06%, 17.40% ± 10.84%, 13.84% ± 8.36% and 25.10% ± 12.16% at 443, 482, 561 and 655 nm, respectively. The highest proportions at the blue and red spectral regions confirm the absorption peaks by Chl-*a* pigment. In sequence, the NAP presented the lowest proportion of the absorption budget with 14.11% ± 4.80% at 443 nm; 14.86% ± 5.27% at 482 nm; 10.07% ± 4.40% at 561 nm and 5.08% ± 2.99% at 655 nm. The peak of NAP absorption in the blue spectral region is typical of detrital or mineral particle which was also verified in BAR2, with 6.85% ± 3.31% and 6.91% ± 3.89% at 443 and 482 nm, respectively, and 5.03% ± 3.77% at 561 nm and 2.99% ± 3.01% at 655 nm. The phytoplankton achieved 4.86% ± 2.30% at 443 nm and 4.24% ± 2.05% at 482 nm,

being higher in the blue spectral region. At 561 nm, the percentage was 2.90% ± 1.65% and at 655 nm, 2.99% ± 3.01%.

Figure 2.4. Ternary plots depicting BAR1 and BAR2 for center OLI bands (a) 443 nm, (b) 482 nm, (c) 561 nm and (d) 655 nm.

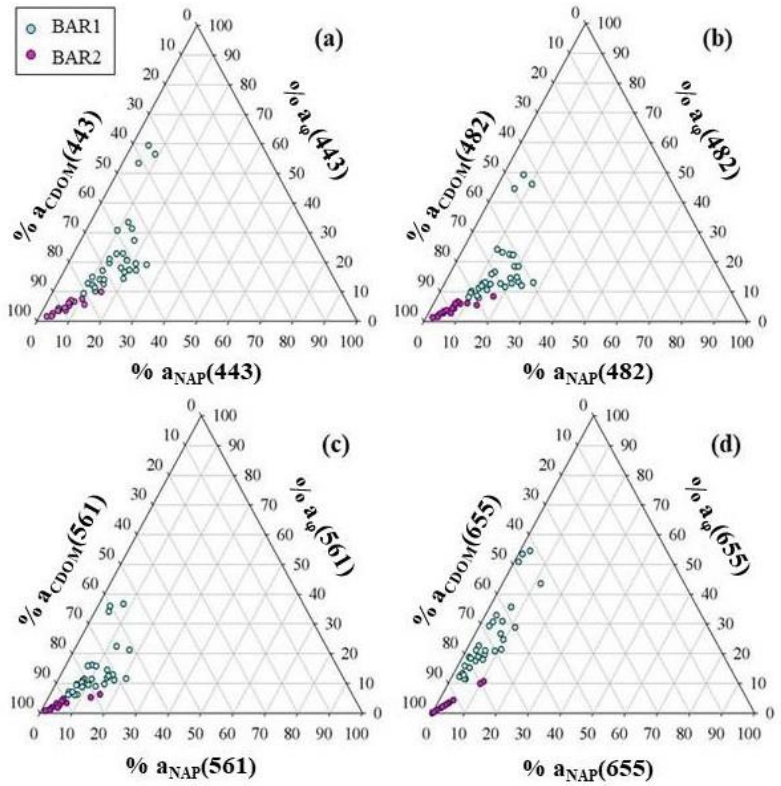

Considering both dataset, the [Chl-*a*] had an average of 77.84 ± 77.15 μg L^{-1} and the organic particles had the highest concentration (4.99 ± 3.96 mg L^{-1}), with the greater part of light absorbed by CDOM.

The average of $k_d(490)$ in BAR1 and BAR2 was 2.80 ± 0.30 m^{-1} (ranging from 1.87 to 3.98 m^{-1}) and 1.79 ± 0.12 m^{-1} (ranging from 1.54 to 2.34 m^{-1}), respectively. The water column was more attenuated in August/2016 than June/2017. Both months are in the dry season; however, 2016 presented the highest mean rate of precipitation from January to June when compared with 2017 over the Bariri reservoir area (Figure 2.1d). The rain carries organic matter, mainly from industrial effluents; wastewater and particulate matter to the Bariri reservoir, as well as facilitates the increasing of organic matter fluxes along the Tietê River from upstream to downstream. The Tietê River is one of the most industrialized basin of São Paulo State and the reservoirs construction promoted the rapid transformation in the land use and land cover, facilitating the pollution problems and accelerating the sedimentation process (Prado *et al.*, 2007). The

concentration of water constituents was higher in August, increasing the process of absorption and backscattering of light and, consequently, showing the highest $k_d(490)$ values.

2.3.3. Assessment of the vertical attenuation coefficient models

Due to the lack of data from turbid inland waters used in the calibration of $k_d(490)$ algorithms, the adjustment for Bariri reservoir can be compromised. The algorithm coefficients developed for a wide range of waters tries to minimize this limitation although it is not a guarantee of success (Lee *et al.*, 2005). For all $k_d(490)$ algorithms, the bands were defined according to the center bands from OLI/Landsat-8, including the blue band at 490 nm that was replaced by 482 nm. The Table 2.3 summarized the statistical results yielded after the application of $k_d(490)$ models.

Table 2.3. Error assessment of $k_d(490)$ models developed for clear, slightly turbid, turbid ocean waters, coastal waters and global waters applied to all dataset of Bariri.

Type	Model	MAPE (%)	RMSE (m^{-1})	*bias* (m^{-1})
Empirical	Morel *et al.*(2007) I	60.96	1.48	-1.21
	Morel *et al.*(2007) II	61.03	1.50	-1.19
	Mueller (2000)	86.46	2.19	-2.12
	Mueller and Tress (1997)	86.15	2.19	-2.11
	Chauhan *et al.* (2003)	82.35	2.04	-1.86
	Werdell (2005)	86.05	2.18	-2.11
	Kratzer *et al.* (2008)	60.62	1.63	-1.52
	Zhang and Fell (2007)	42.90	1.22	-1.07
	Wang *et al.* (2009)	54.04	1.39	-1.15
Semi-analytical	Wang *et al*. (2009) I	46.34	1.31	-1.18
	Wang *et al*. (2009) II	63.68	1.69	-1.59
	Lee *et al.* (2013)	41.04	1.07	-0.90

The empirical models of $k_d(490)$ based on [Chl-*a*] underestimated the results for almost the entire dataset, except for two samples with high values of [Chl-*a*] which were overestimated. The coefficients of the model from Morel *et al.* (2007) were developed for Case I waters, with the optical properties dominated by phytoplankton, therefore, the accuracy of the model in aquatic environments with high rates of CDOM and/or suspended solids is expected to be fail (Zhao *et al.*, 2013). The models from Morel *et al.* (2007) were calibrated with open ocean waters with values of [Chl-*a*] < 2.4

μg L^{-1}, highly discrepant of the values found in Bariri reservoir, resulting in $k_d(490)$ errors of MAPE ~ 61% and RMSE ~ 1.50 m^{-1}.

The empirical models using nL_w spectral ratio developed for ocean open and global waters presented the worst results with MAPE around 80% and RMSE ~ 2 m^{-1}. Mueller (2000); Mueller and Tress (1997), Chauhan *et al*. (2003) and Werdell (2005) models underestimated the results of $k_d(490)$ with *bias* around 2 m^{-1}. The calibration dataset involved waters with values of $k_d(490)$ up to 0.61 m^{-1} whereas in Bariri all dataset varied from 1.55 to 3.98 m^{-1}.

The blue-green ratio $nL_w(490)/nL_w(555)$ or $R_{rs}(490)/R_{rs}(555)$ has a large uncertainties when $k_d(490)$ is greater than 0.25 m^{-1}. The spectral ratio presents an asymptotic value with increasing OSS concentration (Mueller, 2000). Thus, this spectral ratio is not sensitive for the variations in OSS that occurred in turbid inland waters, resulting in significant underestimation of $k_d(490)$. In addition, this spectral ratio does not consider the effects of sun angle changes that decrease the accuracy of empirical algorithms for estimating $k_d(490)$ (Lee *et al.*, 2005).

Aiming to investigate the estimation of $k_d(490)$ from MERIS, Kratzer *et al.* (2008) developed the empirical algorithm from the ratio of 490 nm and 620 nm for a Case 2 water optically dominated by CDOM which showed inversely relation to salinity in Baltic Sea. The Kratzer *et al.* (2008) model applied to all dataset from Bariri presented MAPE of 60.62% and RMSE of 1.63 m^{-1}.

The empirical algorithm developed by Wang *et al.* (2009) combined open ocean and turbid coastal waters (from 0.3 to 0.6 m^{-1}) through a linear regression equation of $R_{rs}(670)/R_{rs}(490)$ ratio that showed better matching of $k_d(490)$ data when the $k_d(490)$ values of calibrated data were higher than 0.3 m^{-1}. The application of this model in Bariri reservoir data resulted in a MAPE of 54.04% and RMSE of 1.39 m^{-1}, yielding underestimated values (bias of -1.15) of $k_d(490)$.

The semi-analytical algorithms of Wang *et al.* (2009) were developed considering the MODIS satellite data and the absorption and backscattering coefficients derived from Lee *et al.* (2002). The algorithm based on the ratio R(667)/R(488) presented MAPE of 46.34% and RSME of 1.31 m^{-1}, while the ratio R(645)/R(488) showed MAPE around 63.68% and RMSE of 1.69 m^{-1}. The OLI sensor does not have a spectral band centered at 488 neither at 667 nm or 645 nm, but at 482 and 655 nm, respectively. Therefore, in both semi-analytical equations, the R(482) and R(655) were used and the

differences found in the results above are explained by the coefficients, which in the first model presented better adjustment than the second model in Bariri reservoir.

The Zhang and Fell (2007) empirical algorithm and the semi-analytical algorithm developed by Lee *et al.* (2013) presented similar performances corresponding to MAPE of 42.90%; RMSE of 1.22 m^{-1} and MAPE of 41.04%; RMSE of 1.07 m^{-1}, respectively. Calibrated with a wide range of environments (0.016 – 4.6 m^{-1}), the Zhang and Fell (2007) model have showed greater correlation for clear waters whereas the Lee *et al.* (2013) algorithm showed the greatest application for turbid waters such as happens for this study site. The difference in errors among these empirical and semi-analytical algorithms could be explained by the use of 655 nm wavelength in Zhang and Fell (2007) model which introduce noise due to the high absorption rate of water in the red wavelength even after corrections in data processing.

The Lee *et al.* (2013) semi-analytical algorithm showed the lowest errors (MAPE = 41.04%; RMSE = 1.07 m^{-1}) for $k_d(490)$ estimation in Bariri reservoir. In inland waters, the regional variability of the OSSs generates significant changes in the attenuation of light process, therefore, the Lee *et al.* (2013) algorithm in considering $a(\lambda)$, $b_b(\lambda)$ and Sun angle resulted in a fewer uncertainties regarding data matching. Besides, the algorithms coefficients derived from numerical simulations reduce the dependence of a specific data range.

Empirical algorithms were developed (results not shown here) from Bariri using all dataset, however the results were not satisfactory, therefore Lee *et al.* (2013) model was chosen for mapping the variability of $k_d(490)$ in the study site.

2.3.4. Assessment of the OLI atmospheric correction product

The evaluation of LaSRC accuracy consisted in the comparison between the OLI-derived R_{rs} product from August/2016 and the R_{rs} calculated from TriOS data in BAR1. The relative percentage errors were 50.09% at 443 nm, 20.68% at 482 nm; 17.24% at 561 nm and 29.64% at 655 nm. The highest errors at the coastal and blue regions are related to the increase of scattering in those regions. The lowest error was verified at green region with 17.24% and, in sequence at red region, the error increased again to 29.64%. The LaSRC accuracy results encountered here are compatible with the atmospheric correction analysis presented in Rodrigues *et al.* (2017) and Bernardo *et al.* (2017).

2.3.5. Application of $k_d(490)$ on OLI/Landsat-8 images

The variability of $k_d(490)$ in Bariri reservoir expressed in OLI/Landsat-8 was presented in Figure 2.5.

Figure 2.5. Spatial distribution of $k_d(490)$ in Bariri reservoir using the semi-analytical model from Lee et al. (2013) considering the months from February to November of 2016. The arrows A and B highlight the reservoir zones near urban centers.

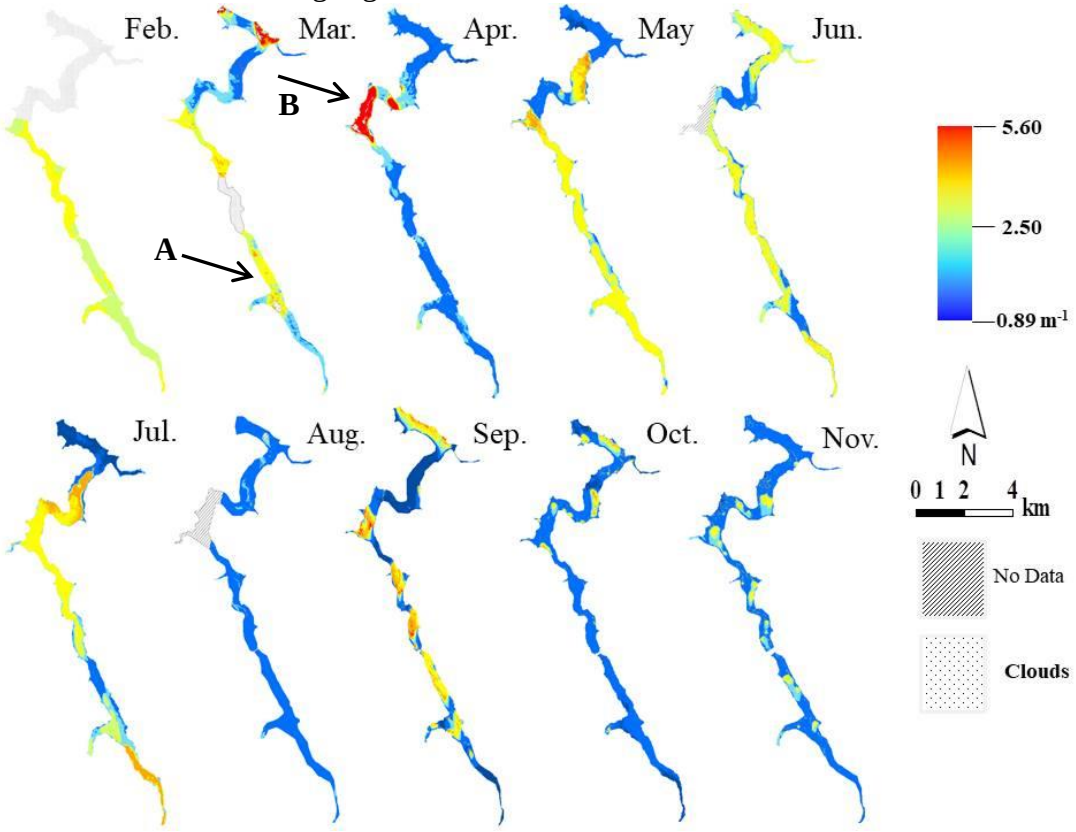

The spatial distribution of Lee *et al.* (2013) in Bariri reservoir was validated from the $k_d(490)$ estimations obtained from the image of 15th August and presented MAPE of 32.54% and RMSE of 0.95 m^{-1}. The errors of $k_d(490)$ estimations from Lee *et al.* (2013) model applied for the all dataset, using the *in situ* R_{rs}, were 41.04% of MAPE and 1.07 m^{-1} of RMSE. The differences between the $k_d(490)$ estimations from *in situ* R_{rs} and R_{rs} from LaSRC are related to the decrease of the variability among the sampling points through the sample size reduction, that in the former case was 48 (all dataset) and in the latter case was 26 (4 sampling points with missing information in the image from August in region highlighted as zone B in Figure 2.5) that presented the lowest errors.

The increase of the percentage error between the OLI-derived R_{rs} at 482 nm used as input of $k_d(490)$ estimation and the $k_d(490)$ estimations for BAR1 was 11.86% and

could be related to IOPs estimations via QAA_v5. The application with no modifications in some empirical steps can affect the QAA_v5 performance in complex optically waters (Watanabe *et al.*, 2016; Li *et al.*, 2016).

The maximum value of $k_d(490)$ was 5.60 m^{-1} in April and the minimum value was 0.89 m^{-1} in September, both in the dry season. In the image from April, specifically in the zone B highlighted by the arrow, an expressive increase of the $k_d(490)$ was observed, which is probably related to the reduction of water velocity favoring the increase of [Chl-*a*] and, in a drastically way, an algal bloom, intensifying the attenuation of light in the water. Along the reservoir, excepting for zone B, the $k_d(490)$ values remained below the mean (Figure 2.6), which was expected for a period of low precipitation, confirming an atypical event in April. In September, the $k_d(490)$ was uniformly distributed around the mean, with values closer the maximum (4.40 m^{-1}) in the northeast region of the reservoir which presents agricultural activities and bare soil areas that facilities the input of external material into the reservoir even in periods of low precipitation. Other regions of high values of $k_d(490)$ were in zone B and another winding points where the water fluxes is slower than in zone A.

Figure 2.6. Boxplot of $k_d(490)$ spatial distribution regarding the months of February to November of 2016 in Bariri reservoir.

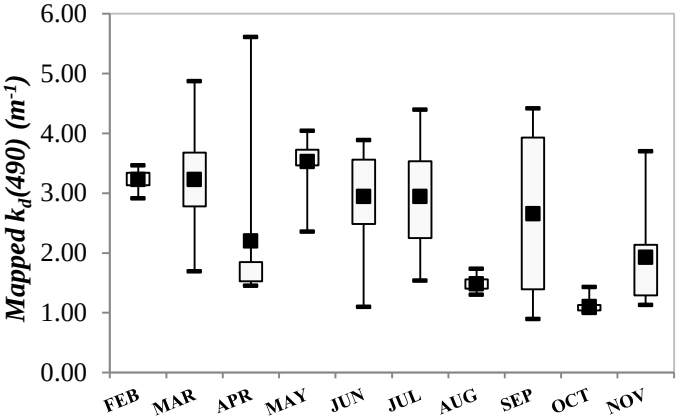

The boxplot in Figure 2.6 summarizes the statistical performance of $k_d(490)$ for each month. In dry season, the $k_d(490)$ values were closer to the maximum in May and June, with the mostly values above the mean and, concomitantly values above 2.50 m^{-1} in zone A. In July and August, the $k_d(490)$ started to decrease with mostly of the values closer to the minimum and below the mean, with also decreasing of $k_d(490)$ in zone A. The precipitation rates were quite smaller in July (~ 3.99 mm) and August (~ 53.83

mm) than in May (~ 125.25 mm) and June (~ 125.43 mm) in conjunction with reducing of $k_d(490)$ in zone A which could be revealed a point source of wastewater.

Unfortunately, the image from August, coincident with the BAR1 field campaign, has no information in the region highlighted as zone B that prevent to show the highest Chl-*a* concentrations in these sampling points which generated high values of $k_d(490)$ as mentioned in section 2.3.1. The mean was 1.48 m^{-1}, with values closer to the minimum, ranging from 1.30 to 1.73 m^{-1}, not corresponding with *in situ* $k_d(490)$. The precipitation rate in August was very low, resulting in low $k_d(490)$ in zone A.

The months of October, November, February and March are representative of wet season, however in October the mean $k_d(490)$ almost coincided with the minimum resulting in low values with some peaks in reservoir northeast and in a winding region.

In November, the increase of $k_d(490)$ was observed with the mean closer to maximum value, presenting some points above 2.50 m^{-1}. In February, with higher precipitation rates than the months previously mentioned, the $k_d(490)$ was around 3.00 m^{-1} even with approximately 30% of the reservoir covered by clouds. In March, the $k_d(490)$ was well distributed around the mean, ranging from 1.69 to 4.87 m^{-1}, with the highest values in northeast and extremely north of reservoir and values above 2.50 m^{-1} in some part of zone B and in zone A.

2.4. Conclusions

After the application of several tests with the $k_d(490)$ estimation models available for a wide range of waters, it was verified that the empiricism does not allowed to estimate the $k_d(490)$ in an accurate way in Bariri reservoir. The uncertainty presented by the empirical models (~80% of MAPE) confirms that the blue/green wavelength ratio is not able to express the $k_d(490)$ variability in an environment dominated by CDOM which was verified in the two surveys realized. The [Chl-*a*] empirical models presented intermediary errors (~ 60% of MAPE) when applied with the aggregated data from the two surveys realized. In BAR1, the [Chl-*a*] were significantly higher than BAR2; the light absorption by CDOM was maintained predominant in both surveys. Among the tested empirical models, the model developed by The Zhang and Fell (2007) was an exception achieving lower errors and statistical results close to those obtained from the semi-analytical models.

The semi-analytical model developed by Lee *et al.* (2013) presented the lowest error (MAPE of 41.04%) among the 12 models analyzed. The coefficients present in Lee *et al.* (2013) model were calibrated from a wide range of waters, filling the lack of the empirical models that are based on a specific dataset. However, the IOPs estimations through the original QAA_v5 can introduce some errors in inland waters due to the optical complexity.

The Lee *et al.* (2013) model was applied in atmospherically corrected OLI/Landsat-8 images (LaSRC) with a relative error percentage difference of 8.50% in relation to the application to all dataset from the R_{rs} obtained *in situ*. Therefore, the atmospheric correction was appropriate to retrieve the $k_d(490)$ and the Lee *et al.* (2013) model was able to highlights the main variations of $k_d(490)$ in an environment dominated by CDOM as the Bariri reservoir, allowing identify the regions with more or less light attenuation and, consequently, the biota modifications that are dependent of the photic conditions in the water column.

The application of $k_d(490)$ model on OLI/Landsat-8 images exhibited important temporal and spatial variability. The spatial variability was verified in points where the sinuosity of reservoir promoted the reduction of water velocity and facilitates the OSS concentrations, increasing the attenuation of light. The temporal variability was linked to significant activities around the reservoir that increase the runoff and the input of external material into the reservoir mainly in periods of high precipitation rates. Besides, the precipitation in wet season promotes the resuspension and carriage of sediments, increasing the attenuation of light.

CHAPTER 3: Remotely sensed estimation of euphotic zone and Secchi disk depths in a CDOM dominated inland waters

3.1. Introduction

The penetration and availability of underwater light are controlling factors of biological (phytoplankton photosynthesis), chemical (nutrient cycling) and physical (heat transfer) processes (Kirk, 1994). The water transparency is an important parameter for environmental monitoring and water quality (Al Kaabi *et al.*, 2016; Alikas & Kratzer, 2017). The freshwater environments provide support for diverse ecosystems and habitats, however they suffer with anthropogenic interference with waste discharge and runoff which drives to changes of the water quality characterized as algal proliferation, eutrophication and increasing of turbidity and reducing of water transparency (Wetzel, 2001; Calijuri *et al.*, 2002; Lira *et al.*, 2009). The water transparency is affected by the optical significant substances (OSS) such as phytoplankton, chromophoric dissolved organic matter (CDOM), non-algal particles (NAP) and the pure water that absorb and/or scatter the downwelling irradiance which diminish with the depth.

The parameters used to quantify the water transparency are the attenuation coefficient [k_d(PAR)] of the photosynthetically active radiation (PAR), the euphotic zone depth (Z_{eu}) and the Secchi disk depth (Z_{SD}). The k_d(PAR) is the exponential decrease of downwelling irradiance with the depth and it is related to Z_{eu}. The Z_{eu} is defined as the depth where the downwelling irradiance of the PAR [E_d(PAR)] achieved 1% of the E_d(PAR) measured at the surface water; assuming that the water column is homogenous, k_d(PAR) and Z_{eu} are related through the equation $Z_{eu} = 4.605/k_d(PAR)$ (Kirk, 1994). In the euphotic zone, there is sufficient light intensity for significant photosynthesis, therefore, the Z_{eu} had been use to provide information of primary production in water bodies and the Z_{eu} changes can depict environmental patterns and anthropogenic impacts (Kirk, 1994; Majozi *et al.*, 2014; Yang *et al.*, 2015; Ma *et al.*, 2016).

The most common and easy way to quantify the water transparency is the Z_{SD}, taken when the black-and-white disk, lowered in water, is no longer viewable by an observer; because the simple and universal method, the Z_{SD} is routinely used for turbidity monitoring, water transparency, estimate the order of magnitude of optical

substances in water and indicate the eutrophic state in water bodies (Binding *et al.*, 2007; Lee *et al.*, 2015; Shang *et al.*, 2016; Alikas & Kratzer, 2017). The Z_{SD} is able to provide in first-hand the water transparency whereas Z_{eu} measures the water clarity more rigorously and generate more reliable results (Lee *et al.*, 2007; Majozi *et al.*, 2014).

In order to estimate the water clarity using remote sensing data, some empirical and semi-analytical models were developed. Empirical models explore the relation between the diffuse attenuation coefficient at 490 nm [$k_d(490)$] and k_d(PAR) to estimate Z_{eu} in coastal waters and turbid lake waters (Zhao *et al.*, 2013; Zhang *et al.*, 2012; Wang *et al.*, 2009). Zhao *et al.* (2013) used MODIS/Acqua/Terra and SeaWiFS satellite-data to understand the light environment in SW Florida coastal waters. Zhang *et al.* (2012) calibrated a simple model to estimate k_d and, further, Z_{eu} in a shallow, turbid Taihu Lake, China using MODIS data and Wang *et al.* (2009) proposed to use a combination of $k_d(490)$ models to improve the accuracy of estimation of $k_d(490)$ and k_d(PAR) products for both turbid and clear waters using MODIS data in Chesapeake Bay.

Lee *et al.* (2007), aiming an approach that avoided parameterizations regarding the wide seasonal and regional bio-optical variations, developed a semi-analytical Z_{eu} model based on k_d(PAR) and the inherent optical properties (IOPs) derived from the quasi-analytical algorithm (QAA; Lee *et al.*, 2002) using SeaWiFS and MODIS satellite data in ocean and coastal waters. Still using the QAA scheme and a mechanistic model to overcome the empirical limitations, Lee *et al.* (2015) proposed a semi-analytical equation to estimate Z_{SD} as an inverse relation of k_d, derived from the IOPs calculated via QAA, at the transparent window of the water body within the visible domain. This mechanist model of Z_{SD} is a new approach of the underwater visibility theory (Preisendorfer, 1986) that aimed to interpret the exactly sighting of Secchi disk in water by the human eye. The Z_{SD} model achieved good performance ($R^2 = 0.96$ and absolute percentage difference of 16.7%) for a wide range of water clarities ($Z_{SD} \sim$ 0.1-30 m) in configuration of OLI/Landsat-8 visible bands (Lee *et al.*, 2016).

From our understanding there are no investigation of water clarity through the Z_{eu} and Z_{SD} parameters using satellite data in inland waters dominated by CDOM, which is an OSS of dissolved organic matter and it is considered an important water quality indicator which affect the primary productivity due to the interference in penetration of PAR into water column of water bodies, reducing the accuracy of water transparency estimation (Zhang *et al.*, 2009). The main goals of this paper were to assess the

performance of models to estimate Z_{eu} and the new Z_{SD} model developed by Lee *et al.* (2015) in CDOM dominant inland waters; investigate how the estimations are affected by this optical water type and comprehend the influences of the seasonality in rainfall terms on Z_{eu} and Z_{SD}. The intermediary product to obtain Z_{eu} and Z_{SD} through the available models, $k_d(490)$, was derived from the semi-analytical equation of Lee *et al.* (2013) for rich-CDOM inland waters through the QAA using the OLI/Landsat-8 with mean absolute percentage error of ~41%. Six Z_{eu} algorithms were tested and the temporal and spatial distributions of the euphotic zone and Secchi disk depths were evaluated.

3.2. Material and Methods

3.2.1. Study Site

The Bariri hydroelectric reservoir (22° 9’ 49.260” S 48° 44’ 21.420” W) is in the middle of the São Paulo State, in Tietê River, being part of the Cascading Reservoir System (CRS) as the second one of a total of six reservoirs (Figure 3.1).

The Bariri reservoir has been in operation since 1969, presenting the smallest flooded area of 63 km² in an average altitude of 450 meters and has serviced the water supply for human use, irrigation and recreation. By the reduced dimension of the reservoir, the operation type is water line with retention time variation from 7 to 24 days (Barbosa *et al*., 1999). The reservoir is situated in a tropical climate with a dry period (April-September) and a wet period (October-March) according to Köppen classification.

The Tietê River traverses the metropolitan region of São Paulo State bringing an amount of wastewater in the downstream direction. The Cascading Reservoir Continuum Concept (CRCC) allows the gradual decrease of nutrients and pollutants along the reservoirs and location and retention time of Bariri reservoir promotes the heterogeneity of the eutrophication levels in upstream to downstream, revealed by the water transparency of the water. The Bariri reservoir is characterized as highly productive water with high average concentrations of total nitrogen (2750 μg L^{-1}), phosphorus (87 μg L^{-1}) and Chl-*a* (55.8 μg L^{-1}) with the phytoplankton community dominated by cyanobacteria (Barbosa *et al*., 1999).

Figure 3.1. Maps showing the location of (a) São Paulo State in Brazilian territory and the path/row of OLI/L8 images which the coordinates of Bariri reservoir are contained, highlighted by the red square; (b) CRS of Tietê River in São Paulo State with the six reservoirs and their respective dams (1 – Barra Bonita; 2 – Bariri; 3 – Ibitinga; 4 – Promissão; 5 – Nova Avanhadava; 6 – Três Irmãos) and (c) Bariri reservoir boundaries with the sampling points of the two field campaigns.

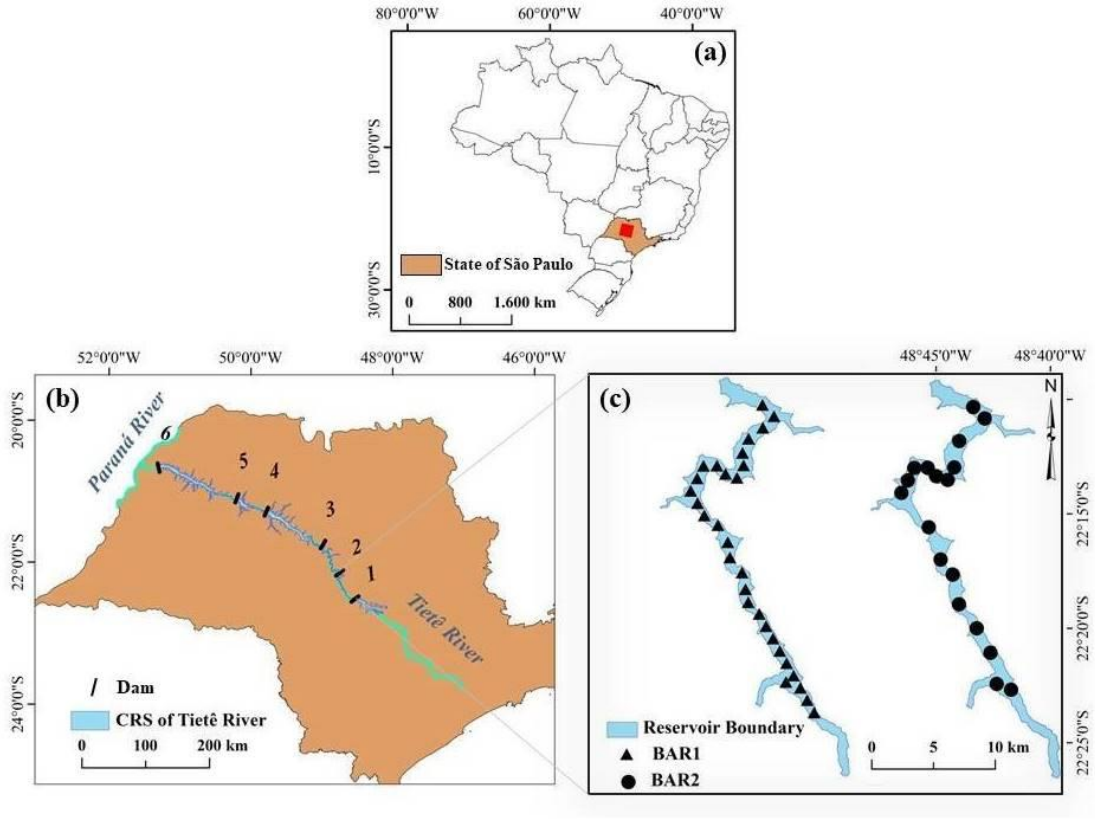

3.2.2. Planning of Sampling and Fieldworks

The establishment of the samples was based on a random stratified sampling method using an annual cycle (2013) of OLI/L8 images acquired at the USGS *website* (www.earthexplorer.usgs.gov). In order to analyze the natural and anthropic variations along the reservoir, the same band of each radiometrically calibrated image (each one with 6 spectral bands) were compressed and submitted to calculation of the mean and, sequentially, of the standard deviation (SD). The SD images were used in a Principal Component Analysis (PCA) for selection of the image with the highest variability, which was sliced for the random stratified sampling (Rodrigues *et al*., 2016).

For Bariri reservoir, 30 sampling points were established ensuring the minimal distance of 1 km between them to avoid clusters. Two fieldworks were carried out in the dry period, being the first one (BAR1) realized from 15 to 18 August 2016 with the 30

sampling points considered and the second one (BAR2), realized from 23 to 24 June 2017 with 12 samples points less than BAR1, maintaining the points which presented high values of OSS concentrations and avoiding the clusters to ensure the spatial variability (see Figure 3.1 for sampling locations). The days of the field campaigns were determined according to the temporal resolution of OLI/Landsat-8 aiming to match the data collection with the satellite overpass the study site. The months of fieldworks were chosen to avoid rainy periods and facilitate the field data collection.

3.2.3. Field Data Collection

During the BAR1 and BAR2, water samples for laboratory analyses, water quality parameters and optical data were collected. The water quality parameters such as depth (m), turbidity (NTU) and Secchi disk depth (Z_{SD}; m) were sampled in both fieldworks. The wind speed (m^{-1}) was measured using a portable anemometer.

The water samples were collected in the field and stored refrigerated in polyethylene bottles to derive the OSSs and IOPs. The OSSs such as the Chl-*a* and the suspended particulate matter (SPM) as well as the inorganic (IPM) and organic particulate matter (OPM) concentrations were obtained from 0.2-0.5L of filtered water and replica in each sample point according to Golterman *et al.* (1978) and the American Public Health Association Protocol (APHA, 1998), respectively. The laboratorial analyses of the IOPs were made from 0.1L of filtered water and replica in each sampling point following the methodology proposed in Bricaud *et al.* (1981) for the absorption coefficient of the CDOM (a_{CDOM}) while for the absorption coefficients of the non-algal particle (a_{NAP}) and the total particulate (a_p), that consists in the sum of a_{NAP} and phytoplankton absorption coefficient (a_φ). The acquisition and analyses were made in accordance with the Transmittance-Reflectance method according to Tassan and Ferrari (1995, 1998, 2002).

The radiometric data were obtained from the two hyperspectral RAMSES sensors, the ARC type with an angle-of-view of 7º used for the radiance measurements and the ACC type with a cosine collector for the irradiance measurements (TriOS, Rastede, Germany). The sky and total radiance data (L_{sky} and L_t, respectively, both in W m^{-2} sr^{-1}) and the downwelling and sky irradiance data (E_d and E_{sky}, respectively, both in W m^{-2}) were taken with the sensors fixed by a steel frame in the boat, in a configuration of 40° from nadir (zenith) and to azimuthal angle of 90° in order to minimize the specular

reflection (Mobley, 1999). The radiometric quantities were used to calculate the remote sensing reflectance according to Equation (3.1).

$$R_{rs}(\lambda) = \frac{L_t(\lambda) - L_{SR}(\lambda)}{E_d+(\lambda)} = \frac{L_t(\lambda) - (\rho L_{sky}(\lambda))}{E_d+(\lambda)} \quad (3.1)$$

where E_d+ is the downwelling irradiance measured at the water surface. The L_{SR} is the surface-reflected radiance and consists in a multiplicative product of L_{sky} and ρ - an effective surface reflectance. The ρ value ($\approx$0.02-0.05) depends on the viewing geometry and spectral variation. In agreement with that, Lee et al. (2010) proposed a calculation approach of R_{rs} as a function of the total remote-sensing reflectance (T_{rs}, ratio of L_t to E_d) and sky remote-sensing reflectance (S_{rs}, ratio of L_{sky} to E_d) for each L_t and L_{sky} scan from the Equation (3.2):

$$R_{rs}(\lambda) \approx T_{rs}(\lambda) - F \times S_{rs}(\lambda) - \Delta \quad (3.2)$$

where F refers to Fresnel reflectance and it was set as 0.021 according to the viewing geometry; Δ is a spectrally constant settled before R_{rs} can be derived (Lee *et al.*, 2010). In oceanic waters, the R_{rs} is negligible in the red and near-infrared wavelengths and Δ can be assumed as zero beyond 700 nm, however, for turbid inland waters, the IOPs have a significant influence in R_{rs}, thus, one alternative is to model the spectral R_{rs} based on the IOPs, and then resolve Δ after comparing modeled R_{rs} and derived R_{rs} from Equation (3.2).

In sequence, the R_{rs} used in estimates model of k_d and, in sequence, estimates models of Z_{SD} and Z_{eu}, must be simulated to the satellite signal at each spectral channel centered at a wavelength (λ = 443; 482; 561; 655 nm). The band simulation consists in the convolution of the radiation signal of TriOS RAMSES hyperspectral sensor and the spectral response function [$F_r(\lambda)$] of the OLI/L8 sensor in wavelength interval of the spectral resolution (Barsi *et al.*, 2014):

$$R_{rs}^{c}(\lambda) = \frac{\int_{x_{min}}^{x_{max}} R_{rs}(\lambda) F_r(\lambda)}{\int_{x_{min}}^{x_{max}} F_r(\lambda)} \quad (3.3)$$

where $R_{rs}^{c}(\lambda)$ is the remote-sensing reflectance simulated at center wavelength; x_{max} and x_{min} are, respectively, the maximum and minimum values of the sensor spectral channel.

According to E_d data, the $k_d(490)$ in both field campaigns was determined as the slope E_d data simulated to satellite signal at spectral channel centered at 482 nm at subsurface depth (z) $[E_d^-(z)]$ (Mobley, 1994):

$$k_d(\lambda, z) = \frac{1}{E_d^-(\lambda)} \frac{dE_d^-(\lambda)}{dz} \quad (3.4)$$

In order to eliminate the noise in the $E_{sky}(\lambda)$ due to changes in the sun illumination condition caused by cloud cover during the $E_d^-(z)$ measurements, a normalization factor was required in all scans. The E_d normalization consists in a division of E_{sky} at first scan $t(z_1)$ to E_{sky} at subsequent scans $t(z_i)$ as factor normalization of the $E_d^-t(z_i)$ according Mishra *et al.* (2005) and Mueller (2000):

$$E'_d(z_i, \lambda) = \frac{E_d(z_i,\lambda) E_{sky}(t(z_1),\lambda)}{E_{sky}(t(z_i),\lambda)} \quad (3.5)$$

where $E'_d(z_i, \lambda)$ is the normalized $E_d^-t(z_i)$.

The E_d data was still used for Z_{eu} determination in both field campaigns by summing the hyperspectral $E_d(\lambda, z)$ from 350 nm to 700 nm, obtaining vertical profiles of $E_{d(PAR)}$ for each sampling point according to Equation (3.6).

$$E_{d(PAR)}(z) = \int_{350}^{700} E_d(z) d\lambda \quad (3.6)$$

In sequence, the Z_{eu} was derived at the depth where the $E_{d(PAR)}(z)$ achieves 1% of the $E_{d(PAR)}$ available at subsurface water $[E_{d(PAR)}(0)]$ or, shortly, as $\frac{E_{d(PAR)}(z)}{E_{d(PAR)}(0)} = 1\%$ (Lee *et al.*, 2005, 2007).

3.2.4. Euphotic Zone Depth Models

The Table 3.1 summarizes the six Z_{eu} models, which cover the semi-analytical and empirical ones.

Table 3.1. Z_{eu} models developed from coastal and ocean waters, slightly turbid ocean waters and turbid lake waters data.

Equations	Model	Calibration Dataset
$z^3 + \frac{K_1{}^2 - K_2{}^2 - 2 \times 4.605 K_1}{K_1{}^2} z^2 + \frac{4.605^2 - 2 \times 4.605 K_1}{K_1{}^2} z + \frac{4.605^2}{K_1{}^2} = 0$	Lee *et al.* (2007)	Coastal and Ocean Waters
$Z_{eu} = \frac{395.92 \times 0.0092}{0.0092 + k_d(490)}$	Zhao *et al.* (2013)	Coastal Waters
$Z_{eu} = \frac{4.605}{k_d(PAR)}$ $k_d(PAR) = 0.8045 k_d(490)^{0.917}$	Wang *et al.* (2009)	Turbid Coastal Waters
$Z_{eu} = \frac{4.605}{k_d(PAR)}$ (I) $k_d(PAR) = 0.896 k_d(490)^{0.873}$	Zhang *et al.* (2012)	Turbid Lake Waters
$Z_{eu} = \frac{4.605}{k_d(PAR)}$ (II) $k_d(PAR) = 0.871 k_d(490)^{0.881}$	Zhang *et al.* (2012)	Turbid Lake Waters
$Z_{eu} = \frac{4.605}{k_d(PAR)}$ (III) $k_d(PAR) = 329.73 \frac{R_{rs}(748)}{\mu_0} + 0.48$	Zhang *et al.* (2012)	Turbid Lake Waters

The semi-analytical model developed by Lee *et al.* (2007) (Z_{eu}_Lee) is a cubic-polynomial equation with the constants based on numerical simulations and two parameters, k_1 and k_2, estimated from the IOPs (*a(490)* and b_b*(490)*) and sun angle (θ_s = 40°). The parameters, k_1 and k_2, are related with $k_{d(PAR)}(z)$, the diffuse attenuation of $E_{d(PAR)}(z)$ in the visible domain (400-700 nm). Considering that Z_{eu} is the layer within which the $E_d(PAR)$ falls 1% of the surface value and $k_d(PAR)$ is approximately constant with the depth (Morel, 1988) the Z_{eu} was related through $k_d(PAR)$ to k_1 and k_2 from the Equation (3.7).

$$Z_{eu} = \frac{4.605}{k_d(PAR)} \tag{3.7}$$

The model generates three solutions, one negative and two positive, but the smallest positive value is consistent with the radiative transfer theory. The IOPs were obtained from the QAA_v5 proposed by Lee *et al.* (2009) (the version 5 was used in this study) with *in situ* R_{rs} as input, simulated at the satellite center channel of reference wavelength (λ_0) of 561 nm, the nearest OLI center band of λ_0 = 55x of QAA_v5.

Zhao *et al.* (2013) aiming to improve the Z_{eu} estimations for the calibration set of coastal waters developed an empirical hyperbolic function based on the relation between *in situ* measures of Z_{eu} and $k_d(490)$, achieving better results for their study site than Z_{eu}_Lee application.

The Z_{eu} values from the empirical models were derived from the correlation between k_d(PAR) and k_d(490) for Z_{eu} estimations in Wang *et al.* (2009) (Z_{eu}_Wang) and in the two first equations of Zhang *et al.* (2012) (Z_{eu}_Zhang_I and Z_{eu}_Zhang_II, respectively). The equation III of Zhang *et al.* (2012) (Z_{eu}_Zhang_III) was calibrated with MODIS data with a channel at the near infra-red spectral region of 748 nm and considered the ratio of $R_{rs}(748)$ and solar zenith angle cosine (μ_0), calculated according to the sampling time, latitude and solar declination. Taking into account the attenuation coefficient dependence on the sun angle and the light angular distribution, the ratio $R_{rs}(\lambda)/\mu_0$ reduces the effect of sun angle on k_d(PAR) estimations. From the k_d(PAR) obtained in Z_{eu}_Wang, Z_{eu}_Zhang_I-III, the Z_{eu} was estimated using the Equation (3.7). The relation used to obtain Z_{eu} from k_d(PAR) has been commonly applied in water quality studies (Ma *et al.*, 2016; Liu *et al.*, 2016; Majozi *et al.*, 2014).

3.2.5. Secchi Disk Depth Model

The Z_{SD} model analyzed in this study was developed by Lee *et al.* (2015) based on the inversion relation between Z_{SD} and k_d. The Z_{SD} estimations require the application of a sequential scheme with three steps, initializing with the IOPs ($a(\lambda)$ and $b_b(\lambda)$) estimations from QAA_v5 (λ_0 = 561 nm); in sequence, as second step, the $k_d(561)$ calculation according to the Lee *et al.* (2013) from the IOPs previously estimated and, finally, as third step, the Z_{SD} calculation from the Equation (3.8).

$$Z_{SD} = \frac{1}{2{,}5(k_d(561))} \ln\left(\frac{|0{,}14 - R_{rs}(561)|}{0{,}013}\right) \quad (3.8)$$

where k_d at 561 nm was the minimal value of attenuation of E_d in the visible domain (443-665 nm) as recommended in Lee *et al.* (2015). The light attenuation in turbid waters is higher in the blue and red spectral regions because the selective absorption (Cairo *et al.*, 2017; Kirk, 1994). In accordance with that, the maximum transmission of light happens at the green spectral region, called the transparency window in the visible domain, justifying the choice of $R_{rs}(561)$ among the OLI center wavelengths.

3.2.6. OLI/Landsat-8 Data Acquisition and Processing

The Landsat 8 Surface Reflectance on-demand data generated by the Landsat Surface Reflectance Code (LaSRC) were obtained in the U.S. Geological Survey platform (*http://earthexplorer.usgs.gov/*). The LaSRC algorithm for atmospheric correction was developed using the Second Simulation of the Satellite Signal in the Solar Spectrum Vectorial (6SV) model. The algorithm uses the OLI Coastal Aerosol Band (0.433–0.450 μm) which works as cover for shorter wavelength as the blue band in previous Landsat and helpful to retrieve aerosol properties (Vermote *et al*., 2016). Pahlevan *et al.* (2017) and Bernardo *et al.* (2016) showed that LaSRC is a consistent product to derive aquatic estimates.

A total of 31 images atmospherically corrected images (Path/Row 221/75 or 220/76) were acquired during the years of 2014, 2015 and 2016. The criteria used for the images choice was attributed to cloud free data over the entire reservoir (images with some parts covered were selected). In 2014, the twelve images were selected; in 2015, nine images were selected with March, November and December images missing; in 2016, ten images were selected with January and December images missing. In order to map the Z_{eu} and Z_{SD} models, surface reflectance images were divided by π to convert them into R_{rs} and rescaled by a factor scale of 0.0001 to convert to the 0 to 1 range (Moses *et al.*, 2012; USGS, 2018).

The Z_{eu} model with the best performance and the Z_{SD} model from Lee *et al.* (2015) were applied to the time-series of LaSRC images selected to obtain the spatial distribution of depths of the euphotic zone and the Secchi disk. The Figure 3.2 displayed the flowchart of the of Z_{eu} and Z_{SD} spatialization.

Figure 3.2. Flowchart showing the sequential steps followed to mapping Z_{SD} and Z_{eu}.

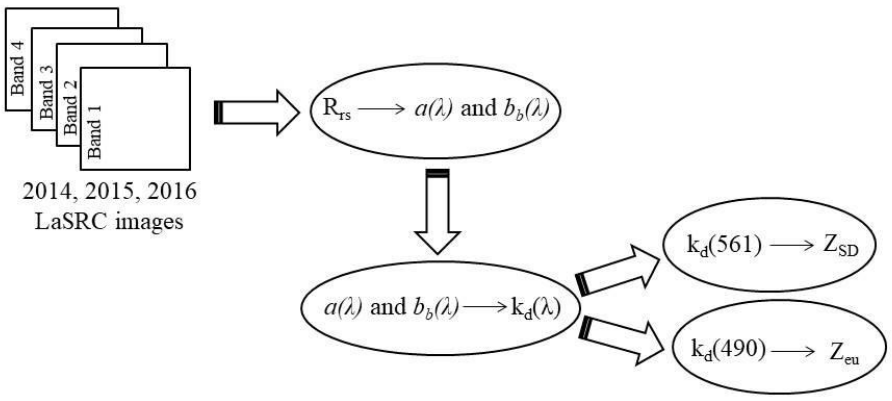

The R_{rs} of first four bands of LaSRC time-series images were used in the equations in original configuration of QAA_v5 (Lee *et al.*, 2009) in order to obtain the $a(\lambda)$ and $b_b(\lambda)$ images. The $a(490)$ and $b_b(490)$ and $a(561)$ and $b_b(561)$ images were used to generated the $k_d(490)$ and $k_d(561)$ images, respectively, from the semi-analytical model proposed by Lee *et al.* (2013). These two steps enable the mapping of Z_{SD} using the semi-analytical equation by Lee *et al.* (2015) and the mapping of Z_{eu} from any model tested in this study.

The Z_{SD} model and Z_{eu} model best fitted for Bariri reservoir were validated through the satellite image from August 15th 2016, correspondent to the first day of BAR1. In the same way, the LaSRC accuracy in Z_{eu} and Z_{SD} estimations were evaluated from the analysis between the R_{rs} converted images with the R_{rs} calculated from TriOS data in BAR1.

3.2.7. Statistical Analysis and Accuracy Assessment

Statistical analyses, including calculations of the maximum, minimum and average values and linear and non-linear regressions were performed. The Z_{eu} and Z_{SD} analyzed models were applied for BAR1 and BAR2 datasets. The Root Mean Square Error (RMSE), Unbiased Absolute Percentage Error (ε) and the *bias* were used to assess the accuracy of the models.

$$\mathrm{RMSD} = \sqrt{\frac{1}{j}\sum_{i=1}^{j}\left(x_{est,i} - x_{mea,i}\right)^2} \tag{3.9}$$

$$\varepsilon = \frac{200\%}{j}\sum_{i=1}^{j}\frac{|x_{est,i} - x_{mea,i}|}{x_{est,i} + x_{mea,i}} \tag{3.10}$$

$$bias = \frac{1}{j}\sum_{i=1}^{j}\left(x_{est,i} - x_{mea,i}\right) \tag{3.11}$$

where x_{est} and the Z_{SD} and Z_{eu} estimated values and x_{mea} is the *in situ* measures of Z_{SD} and Z_{eu}.

3.3. Results

3.3.1. In situ Measurements

The water color in BAR1 was green in most of the sampling points whereas in BAR 2, the water was brownish. The sky during the field campaigns was in most

favorable with sunny days with the exception of some period of overcast in BAR1. The wind speed (m s^{-1}) ranged from 0 to 8 among the field campaigns with the maximum value in BAR1 that presented average of 3.47 $\pm$ 1.80 m s^{-1} and 3.10 $\pm$ 2.00 m s^{-1}.

The *in situ* R_{rs} spectral curves are in Figure 3.3. The spectral feature of BAR1 was predominant by Chl-*a* pigment influence with a significant absorption at 680 nm and two peaks of reflectance at 550-570 nm and 710 nm, corresponding to typical waters with high phytoplankton concentrations. At the green spectral region, the pigments assume the minimal absorption and all the particulate matter play the major role in reflectance. The sampling points with the highest values of Chl-*a* concentration ([Chl-*a*]) presented a peak of absorption at 440 nm. The dip verified at 625 nm is associated with the phycocyanin pigment that is present mainly in cyanobacteria (Majozi *et al.*, 2014; Gitelson *et al.*, 2007). The R_{rs} magnitude in BAR2 was lower than BAR1 due to the OSS concentrations reduction (see Table 2). The CDOM dominated the light absorption process in both field campaigns (67.74% $\pm$ 9.98% in BAR1 and 88.85% $\pm$ 5.70% in BAR2 at 490 nm) and it was verified in BAR1 with the lower R_{rs} at 400-500 nm while in BAR2, the R_{rs} curves assumed a flat feature at $< \sim$ 600 nm, resulted of a CDOM-rich water with other substances influence (Binding *et al.*, 2008; Brezonik *et al.*, 2015).

Figure 3.3. The R_{rs} spectra for BAR1 (a) and BAR2 (b) surveys.

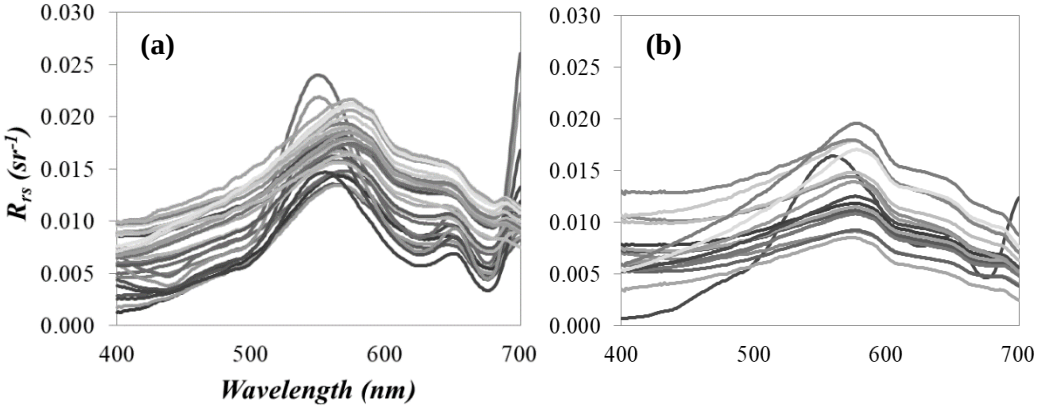

The Table 3.2 presents the summary of *in situ* optical properties. The variability among the parameters in BAR1 was expressively higher than in BAR2. The water depth presented a range from 5.60 to 19.60 m (11.43 $\pm$ 4.32 m) in BAR1 and a range from 4.70 to 21.20 m (12.65 $\pm$ 4.13 m) in BAR2, showing a slight difference in water level among the field campaigns. The OSS concentrations are higher in BAR1 than BAR2,

with a drastic decrease of [Chl-*a*] mean from 119.76 ± 96.43 μg L^{-1} to 7.99 ± 3.27 μg L^{-1} and a decrease of [SPM] from 8.40 ± 4.64 mg L^{-1} to 1.59 ± 0.44 mg L^{-1}. The absorption process by the organic matter also decreased with a_{CDOM} mean of from 1.57 ± 0.37 m^{-1} to 1.06 ± 0.50 m^{-1} and, in the same way, the $k_d(490)$ reduced from 2.80 ± 0.30 m^{-1} to 1.79 ± 0.12 m^{-1} in BAR1 and BAR2, respectively. The reduction of optical substances in water reduced the turbidity from 16.60 ± 7.61 NTU in BAR1 to 5.72 ± 1.25 NTU in BAR2. From the decreasing of turbidity, the water clarity in Bariri reservoir increased from 2016 to 2017 that can be confirmed by the increasing of Z_{SD} and Z_{eu}. The Z_{SD} presented in BAR1 a mean of 1.16 ± 0.23 m and in BAR 2, the mean Z_{SD} increased 0.9 m (2.06 ± 0.19 m). In the same way, the Z_{eu} mean in BAR1 of 2.52 ± 0.29 m increased to 3.63 ± 0.47 m.

Table 3.2. Summary of statistical parameters of the optical properties acquired in BAR1 and BAR2 showing the minimum, maximum, mean, standard deviation (SD) and coefficient of variation (CV). CV = SD/mean.

Field Campaign		**Wind Speed ($m\ s^{-1}$)**	**Water Depth (m)**	**Z_{SD} (m)**	**Zeu (m)**	**Turbidity (NTU)**	**$k_d(490)$ (m^{-1})**	**[Chl-*a*] (μg L^{-1})**	**[SPM] (mg L^{-1})**	**$a_{CDOM}(490)$ (m^{-1})**
BAR1 (N = 30)	Min	0.00	5.60	0.50	1.59	7.80	1.87	25.67	3.60	0.92
	Max	8.00	19.60	1.60	2.88	80.90	3.98	709.89	40.33	2.74
	Mean	3.47	11.43	1.16	2.52	16.60	2.80	119.76	8.40	1.57
	S.D.	1.80	4.32	0.23	0.29	7.61	0.30	96.43	4.64	0.37
	C.V.	51.73%	38.00%	20.03%	12.00%	45.82%	10.69%	80.52%	55.25%	23.73%
BAR2 (N = 18)	Min	0.00	4.70	1.60	2.22	3.48	1.54	3.82	0.20	0.18
	Max	6.50	21.20	2.50	4.03	8.80	2.34	19.11	2.60	2.07
	Mean	3.10	12.65	2.06	3.63	5.72	1.79	7.99	1.59	1.06
	S.D.	2.00	4.13	0.19	0.47	1.25	0.12	3.27	0.44	0.50
	C.V.	65.10%	33.00%	9.31%	13.00%	21.92%	6.47%	40.90%	27.92%	47.84%

3.3.2. Z_{eu} evaluation using in situ data

The Table 3.3 relates the errors found in the application of the Z_{eu} models for the Bariri dataset.

To test the Z_{eu} models, with the Z_{eu}_Lee exception, it was necessary estimates $k_d(490)$ previously. For this, some $k_d(490)$ models were tested using as input data collected in the field campaigns in order to find the best model fitted for Bariri reservoir. The results showed that the semi-analytical model developed by Lee *et al.* (2013) had the lowest errors (MAPE = 41.04%; RMSE = 1.07 m^{-1}). The $k_d(490)$ was derived from IOPs ($a(\lambda)$ and $b_b(\lambda)$) by applying the QAA_v5 scheme, considering the sun angle, that makes the uncertainties regarding the data matching reduce. Therefore,

after the analysis among the $k_d(490)$ models tested, the one developed by Lee *et al.* (2013) was chosen to mapping the variability of $k_d(490)$ and to support the mapping of Z_{eu} and Z_{SD} in Bariri reservoir.

Table 3.3. Errors assessment of Z_{eu} models developed for ocean, costal, slightly turbid ocean and turbid lake waters that were tested for Bariri dataset.

Equations		Model	Validation Dataset		
			BAR1	**BAR2**	**Aggregated**
$z^3 + \frac{K_1{}^2 - K_2{}^2 - 2 \times 4.605 K_1}{K_1{}^2} z^2 + \frac{4.605^2 - 2 \times 4.605 K_1}{K_1{}^2} z + \frac{4.605^2}{K_1{}^2}$		Lee *et al.* (2007)	RMSD (m) ε (%) *bias* (m)	1.26 37.85 1.19	1.87 39.55 1.74	1.40 35.11 1.18
$Z_{eu} = \frac{395.92 \times 0.0092}{0.0092 + k_d(490)}$		Zhao *et al.* (2013)	RMSD (m) ε (%) *bias* (m)	0.46 15.12 -0.34	0.88 19.66 -0.38	0.64 16.76 -0.33
$Z_{eu} = \frac{4.605}{k_d(PAR)}$	$k_d(PAR) = 0.8045 k_d(490)^{0.917}$	Wang *et al.* (2009)	RMSD (m) ε (%) *bias (m)*	1.24 36.38 1.13	1.93 40.62 1.55	1.53 37.91 1.28
	(I) $k_d(PAR) = 0.896 k_d(490)^{0.873}$	Zhang *et al.* (2012)	RMSD (m) ε (%) *bias (m)*	0.94 29.04 0.82	1.44 31.68 1.55	1.15 29.99 0.90
	(II) $k_d(PAR) = 0.871 k_d(490)^{0.881}$		RMSD (m) ε (%) *bias (m)*	1.02 31.11 0.90	1.56 33.90 1.17	1.24 32.12 1.00
	(III) $k_d(PAR) = 329.73 \frac{R_{rs}(748)}{\mu_0} + 0.48$		RMSD (m) ε (%) *bias (m)*	0.78 30.65 -0.08	1.36 29.46 0.22	1.03 30.22 0.024

The Z_{eu}_Lee presented RMSD = 1.40 m, ε = 35.11% and *bias* = 1.18 m when applied for Bariri all dataset (aggregated = BAR1 + BAR2). The errors were considered high among the other analyzed models. Despite the model have been developed from a semi-analytical scheme with the R_{rs} *in situ* data, the empirical models showed better matching with Z_{eu} data in Bariri reservoir.

The Z_{eu}_Lee model was applied to ocean and coastal productive waters with Z_{eu} ranging among ~ 4.30 to 82 m achieving satisfactory agreement between measured and estimated data. However, for turbid inland waters dominated by CDOM as Bariri reservoir with Z_{eu} ranging from 1.59 to 4.03 m, the Z_{eu}_Lee did not fit so well and overestimated Z_{eu} in all sampling points. Some authors in order to improve the IOPs estimations in turbid inland waters parameterized some empirical phases and the reference wavelength of QAA (Li *et al.*, 2016; Yang, *et al.*, 2013; Watanabe *et al.*, 2016). In contrast with that, the $k_d(490)$ estimations obtained from Lee *et al.* (2013) and also dependent on IOPs estimations through the semi-analytical model no parameterize achieved the best results in comparison with the empirical ones when applied for Bariri all dataset.

The radiative transfer approach used in k_d calculation (Lee *et al.*, 2005; Lee *et al.*, 2013) is consistent with the definitions about the nature variations of k_d, considered as an apparent optical property (AOP) (Kirk, 1994). Highly dependent on zenithal sun angle and IOPs, the semi-analytical k_d ensure the adjustment in light field structure changes and the contributions of absorption coefficients of pure water (a_w) and other optical constituents (a) that affect the scattering coefficients of pure water (b_{bw}) and other optical constituents (b_b), reducing, for instance, errors in longer wavelengths (600-800 nm) due to high a_w (Lee *et al.*, 2018).

The Z_{eu}_Lee model was applied to coastal waters with optical environmental significantly affected by CDOM and suspended matter and showed larger errors relative to *in situ* data. The mismatch was associated to the k_d algorithm applicability that derived the Z_{eu} values and the algorithm parameterization. The k_d model used was also the Lee *et al.* (2013) model but in the formula version from 2005, without the extension of the minimal wavelength used in equation development that aimed in amplify the waters range application (Zhao *et al.*, 2013).

The Z_{eu}_Zhao developed for turbid coastal waters (water depth ranged between 2.5-20 m) presented the lowest errors with RMSD = 0.64 m, ε = 16.76% and *bias* = -0.33 m when applied for Bariri all dataset. The empirical model explored the relation between $k_d(490)$ and Z_{eu} measured *in situ*. The success of results for aggregated data can be explained by the similar optical constituents in water. The Z_{eu} measures were taken in data stations that showed variations in spectral shapes covering waters with optical properties influenced by allochthonous source of CDOM and waters with significant amount of absorption and scattering processes, presenting $k_d(490)$ values *in situ* from 0.03 to 1.29 m^{-1}. In analyzing all dataset of Bariri reservoir, the [Chl-*a*] had an 77.84 $\pm$ 77.15 μg L^{-1} with organic particles predominance and the greater part of light absorbed by CDOM indicating a multiple external source of organic matter and the $k_d(490)$ range found was 1.55-3.98 m^{-1}. Although the Bariri is more turbid than the calibration dataset in Zhao *et al.* (2013), the Z_{eu}_Zhao showed a significant matching, higher for BAR1 ($1.59 \leq Z_{eu} \leq 2.88$ m) than BAR2 ($2.22 \leq Z_{eu} \leq 4.03$ m) which showed some disperse sampling points.

The empirical model Z_{eu}_Wang had the worst performance for Bariri dataset (RMSD = 1.53 m, ε = 37.91% and *bias* = 1.28 m) with values in general overestimated. The k_d(PAR) are related to $k_d(490)$ through an *in situ* data with $k_d(490)$ ranging from

0.35 m^{-1} to 6.6 m^{-1} and turbid coastal waters more influenced by phytoplankton and suspended sediment and phytoplankton absorption predominant (Wang *et al.*, 2009). Although the range of $k_d(490)$ values covers the range found in Bariri dataset, the equation coefficients calibrated for different optical environment showed a limitation of the model application in turbid inland waters. The equation to estimate Z_{eu} also did not perform well in turbid inland waters in a Japan Lake, achieving relative error above 100% (Yang *et al.*, 2015).

The equations available in Zhang *et al.* (2012) when applied with Bariri dataset resulted in intermediary values of errors regarding other evaluated models with RMSD = 1.15 m, ε = 29.99% and *bias* = 0.90 m for Z_{eu}_Zhang_I; RMSD = 1.24 m, ε = 32.12% and *bias* = 1.00 m for Z_{eu}_Zhang_II and RMSD = 1.03 m, ε = 30.22% and *bias* = 0.024 m for Z_{eu}_Zhang_III. The Z_{eu}_Zhang_I and Z_{eu}_Zhang_II are simple optical models based on the correlation between the k_d(PAR) measured and $k_d(490)$ estimated by an empirical relation using the ratio $R_{rs}(670)/R_{rs}(490)$ calibrated for turbid inland waters.

The coefficients in Z_{eu}_Zhang_I equation showed slightly better results than the ones used in Z_{eu}_Zhang_II. The Z_{eu}_Zhang_III equation used the $R_{rs}(748)/\mu_0$ because the significant correlation between the near-infrared wavelength and k_d(PAR), that is 97.5% explained by inorganic particles in water, and to reduce the sun angle effect. However, the results were not so different from the two former equations. The different bio-optical conditions of Bariri reservoir in relation to the extremely turbid waters, dominated by NAP, increased the mismatch between the Z_{eu} estimations and Z_{eu} measured. Furthermore, the $k_d(490)$ equation, available in Zhang *et al.* (2012), used in k_d(PAR) equations was applied for Bariri aggregated data and produced large uncertainties, which maximized the errors in Z_{eu} estimations.

The application of Z_{eu} models in BAR1, BAR2 and the aggregated dataset presented few differences in results. BAR1 showed slightly lowest errors than BAR2 and it can be explained by the highest OSS concentrations in BAR1 than BAR2 once the models were based on the IOPs (Lee *et al.*, 2007) and $k_d(490)$ which is also determined by absorption and scattering processes. The Z_{eu} estimations (just Z_{eu}_Zhang_I was considered from Zhang *et al.* (2012) due to the lowest errors presented) were plotted against the Z_{eu} measured from *in situ* data for Bariri aggregated data (Figure 3.4). The estimations of Z_{eu}_Zhao were closer to the 1:1 line and it was used to mapping the euphotic zone in Bariri reservoir.

Figure 3.4. Comparison between derived-Z_{eu} from *in situ* data and those estimated from Z_{eu} models analyzed.

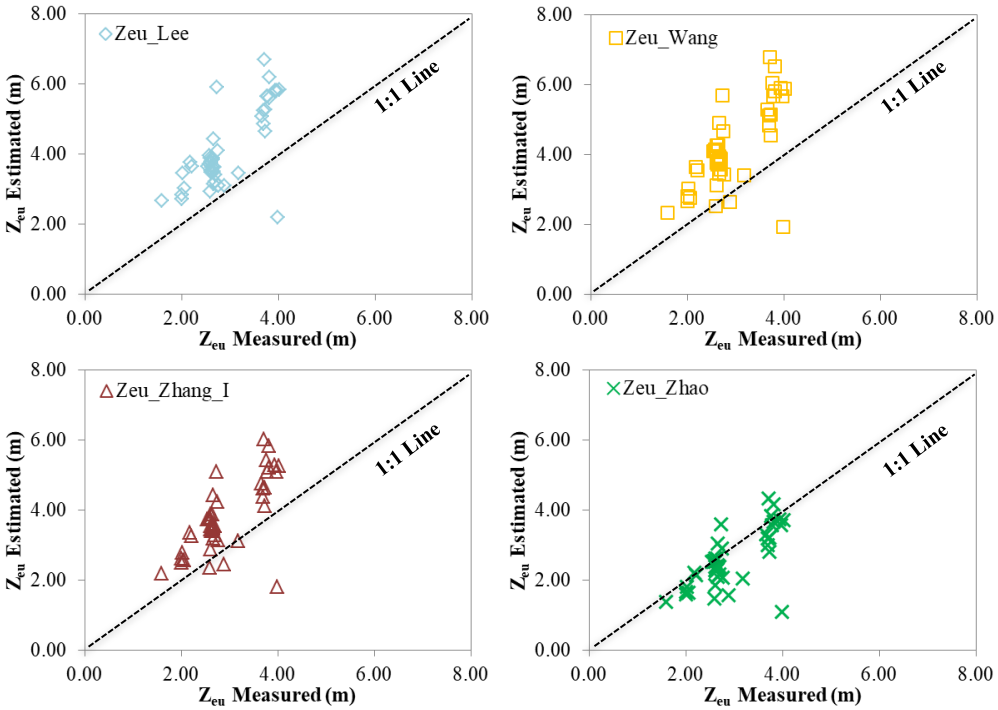

3.3.3. Z_{SD} evaluation using in situ data

The $k_d(561)$ intermediary products to obtain Z_{SD} semi-analytical equation (Lee *et al.*, 2015) showed some uncertainties for Bariri dataset. When the k_d model (Lee *et al.*, 2013) was applied, the errors were almost the same with RMSD = 0.53 m^{-1}, ε = 34.72% and *bias* = - 0.41 m^{-1} for BAR1; RMSD = 0.31 m^{-1}, ε = 31.66% and *bias* = - 0.17 m^{-1} for BAR2 and RMSD = 0.47 m^{-1}, ε = 33.61% and *bias* = 0.33 m^{-1} for Bariri all dataset.

The errors obtained in Z_{SD} estimations are in Table 3.4. The errors showed a large variability among the data sets with the lowest errors for BAR 1 and extremely large errors for BAR2.

Table 3.4. Errors assessment of Z_{SD} (Lee *et al.*, 2015) considering the two field and the aggregated data.

Dataset	RMSD (m)	*bias* (m)	ε (%)
BAR1	0.41	-0.18	34.10
BAR2	1.39	-1.30	97.70
Aggregated	0.90	-0.12	57.10

The Z_{SD} results in BAR2 presented highly underestimation in relation to BAR1 and Bariri all dataset. Rodrigues *et al.* (2017) tested the Z_{SD} model performance in native form in Nova Avanhadava reservoir (downstream to Bariri reservoir) for three different

data groups, the first and third group were characterized by the slight dominance of inorganic particles whereas the second one showed a higher CDOM proportion. The group with higher CDOM influence presented the highest errors in Z_{SD} estimations (RMSD = 1.18 m and *bias* = - 1.00 m) in relation to others influenced by inorganic matter (RMSD and *bias* equivalent to 0.55 m and -0.35 m, respectively, for the first group; 0.99 m and -0.90 m, respectively, for third group). Aiming to improve the results, Rodrigues *et al.* (2017) re-calibrated some empirical steps in QAA_v5 and the uncertainties in Z_{SD} estimations were slightly reduced, more significantly in first and third data group than second one, which led to Z_{SD} underestimations.

Lee *et al.* (2016) using the same algorithm and OLI bands for Z_{SD} varying from ~ 0.1 – 30 m covering clear oceanic and turbid coastal waters, achieved R^2 = 0.96 and unbiased absolute percent difference of 16.7% and 18%. However, the Z_{SD} accuracy for Bariri environment was significantly compromised.

3.3.4. Assessment of LaSRC

The LaSRC have been used successfully to mapping water quality (Bernardo *et al.*, 2016; Concha & Schott, 2016; Rodrigues *et al.*, 2017). The evaluation of LaSRC accuracy consisted in the comparison between R_{rs} from TriOS simulated to OLI bands and the R_{rs} derived from the reference image of August/2016 for the sample points raised in the same day of satellite overpass day. The highest variability in matching the R_{rs} data was at 443 nm and one sample point was chosen to show the LaSRC performance (Figure 3.5a-b).

Figure 3.5. The spectral distribution of the sample points in R_{rs} *in situ* and R_{rs}_LaSRC derived (a) and the R_{rs}_LaSRC derived performance in relation to R_{rs} *in situ*.

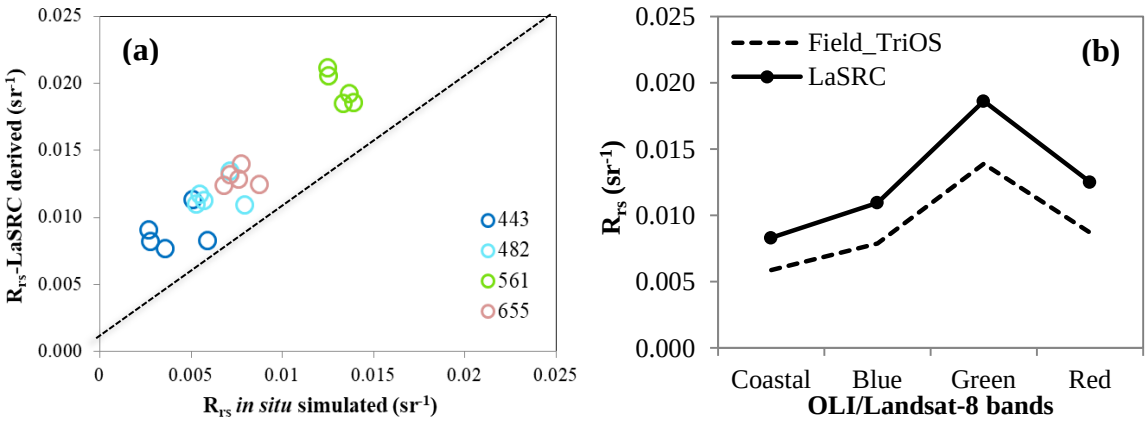

At 443 nm and 482 nm, the errors were the highest with ε = 78.9% and ε = 60.9%, respectively. At 561 nm, the error decreased (ε = 39.4%) and increased again at 655 nm (ε = 53.02%). The highest errors at the coastal and blue regions are related to the increase of scattering in those regions.

3.3.5. Rainfall Data

As depicted in Figure 3.6a, BAR1 and BAR2 were realized in periods of low monthly precipitation rate with 53.83 mm and 29.03 mm in comparison to annual average of 171.10 mm in 2016 and 164.31 mm in 2017 registered in Bariri reservoir, respectively. These values are expected once they occurred in the dry period. In BAR1 period (from 15 to 18 of August of 2016), the first day of surveying data in Bariri reservoir was affected by rainfall at night period and it was verified the increase of turbidity mainly in the two last days of the field campaign where the sampling points presented the water color predominantly green. In BAR2 period (23 and 24 of June of 2017), the monthly precipitation rate was lower than in BAR1 with no rainfall events during the surveying.

Figure 3.6. Graphics of monthly average of (a) rainfall (mm) data for Bariri reservoir, obtained from NASA's GIOVANNI (TRMM Data Product; Spatial Resolution of .0.25º; Monthly Temporal Resolution) database between 2014 and 2017. In 2017, the precipitation data were available just until October and (b) the flow rate ($m^3\ s^{-1}$) of Bariri reservoir in the period 2014-2017 available in the SAR/National Water Agency (*http://sar.ana.gov.br/MedicaoSin*).

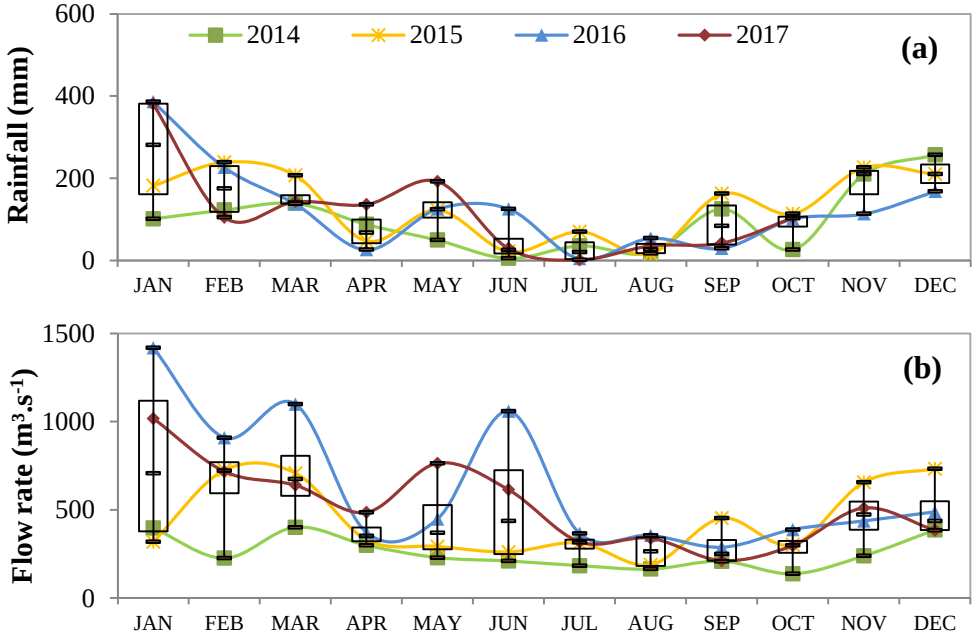

The precipitation achieved the lowest values in June/2014 (5.10 mm), August/2015 (16.77 mm) and July of 2016 (3.98 mm) and 2017 (1.56 mm). The wet months showed the monthly average nearest the maximum values, mainly in January when the precipitation rates achieved ~ 380 mm in 2016 and 2017. In turn, January of 2014 showed the lowest precipitation (101.26 mm), lower than the average of 262.38 mm as well as 2015, with 181.61 mm in January. The highest precipitation in 2015 was in February (238.94 mm) and significant rainfall was observed in September, October and November in relation to other years.

The pattern in the shape of precipitation lines in 2016 and 2017 were quite similar with the exception in May-June/2016 and April/2017 which presented expressive rainfall amount in the southeastern south-center in May/2016 and April/2016 and rainfall above the mean in São Paulo State in June/2016 according the Weather Prevision Center and Climate Studies (available in *http://infoclima.cptec.inpe.br*). The precipitation rates were 125.25 mm, slightly higher than monthly average (122.47 mm), in May/2016 and significant value of 125.42 mm in June/2016, compared with the annual average of 45.22 mm. In April/2017, the precipitation rate was 136.20 mm whereas the annual average for this month was 74.32 mm.

The lowest values were verified in 2014 even for the wet period (exception of November and December months). The Tietê River received only about one-sixth of the usual amount of rain and was classified as extremely dry situation according to Standardized Precipitation Index (SPI), presenting the most severe drought with seven months of duration in 2014 which implied directly in water supply problems (Gomes *et al.*, 2017-a; Coelho *et al.*, 2015; NASA, 2015). The reservoirs in Tietê River dwindled from 3 to 5% of its reservoirs storage capacity (Coelho *et al.*, 2015) reducing the flow rate in Bariri reservoir in the entire year of 2014 which remained above the mean (Figure 3.6b). The flow rate in 2014 presented the lowest values in relation to the subsequent years (exception of January/2015) with the minimum value of time-series of 136.57 $m^3\ s^{-1}$ in October. The annual average for October month was 280.74 $m^3\ s^{-1}$. The flow rate maximum value was 1419.23 $m^3 s^{-1}$ in January/2016. The water flow delineation was according to a water line reservoir, maintaining the water retained in months with less precipitation and in the period of the drought.

3.3.6. Z_{eu} using satellite-derived data

The Figure 3.7 presented the spatial and temporal variability of Z_{eu} in Bariri reservoir expressed in OLI/Landsat-8 images. The annual cycle of available LaSRC images in 2014, 2015 and 2016 were used. Two images of each period (dry and wet) were chosen to show the Z_{eu} variation in Bariri reservoir and boxplot graphic were constructed to analyze the statistical performance of Z_{eu} in each month of the studied period (Figure 3.8). The criteria of images choice presented in this study was the months, at least two for period, with available images simultaneously in 2014-2016 and not sequentially in order to improve visually the Z_{eu} variability. Therefore, the February, May, August and October were the months, which met the conditions mentioned above.

Figure 3.7. Spatial distribution of Z_{eu} using the model based on Zhao *et al.* (2013) for February, May, August and October months of (a) 2014, (b) 2015 and (c) 2016. The A and B arrows highlight zones which presented high variability in Z_{eu} values among the images analyzed.

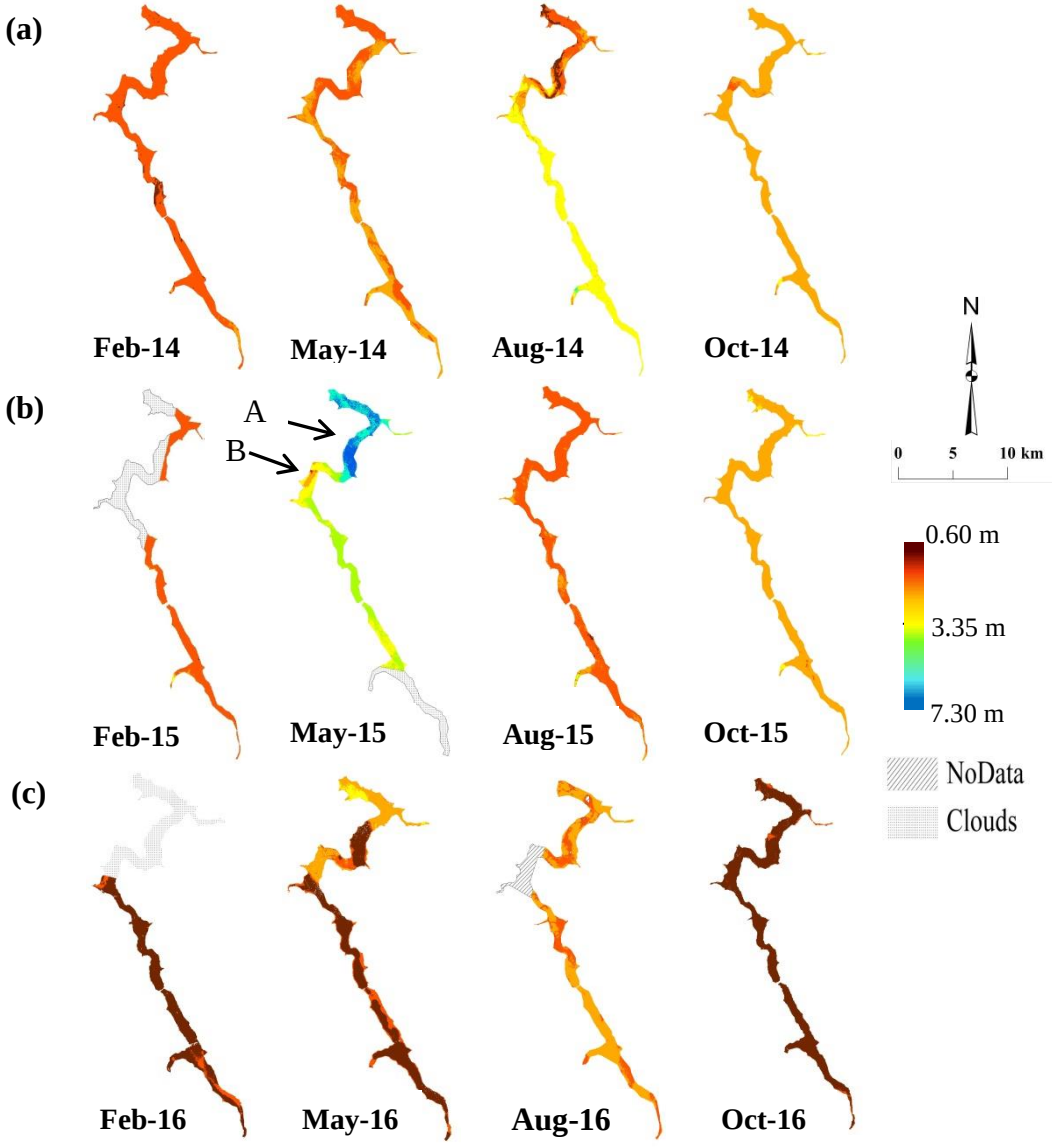

The maximum and minimum Z_{eu} values were 7.30 m in May-2015 and 0.60 m in June-2014, both in the dry season (Figure 3.8a-b). The arrows highlight two zones (A and B) in Bariri reservoir which presented variability between the analyzed images. The zone A showed low Z_{eu} values, except for May-15 image where the Z_{eu} were high. The May-2015 image was marked by atypical rainfall (122.8 mm) equivalent to the monthly average for the 2014-2017 period (Figure 3.6a), increasing the reservoir water level and, possibly, the water velocity in this zone, reducing the optical component concentrations which, in turn minimize the water turbidity; a high Z_{eu} variability (from 3.25 to 7.32 m) can be observed in this month (Figure 3.8b). The zone B presented significantly low Z_{eu} in relation to zone A taking into account the proxy among them; the stain aspect in zone B can be related to an external increment which increased the turbidity punctually (Figure 3.7b). The months of May and June presented the Z_{eu} well distributed around the mean (Figure 3.8b). In February and October, the Z_{eu} average was 1.76 m and 2.77 m, respectively.

Figure 3.8. Boxplot of Z_{eu} spatial distributions in Bariri reservoir for 2014 (a), 2015 (b) and 2016 (c).

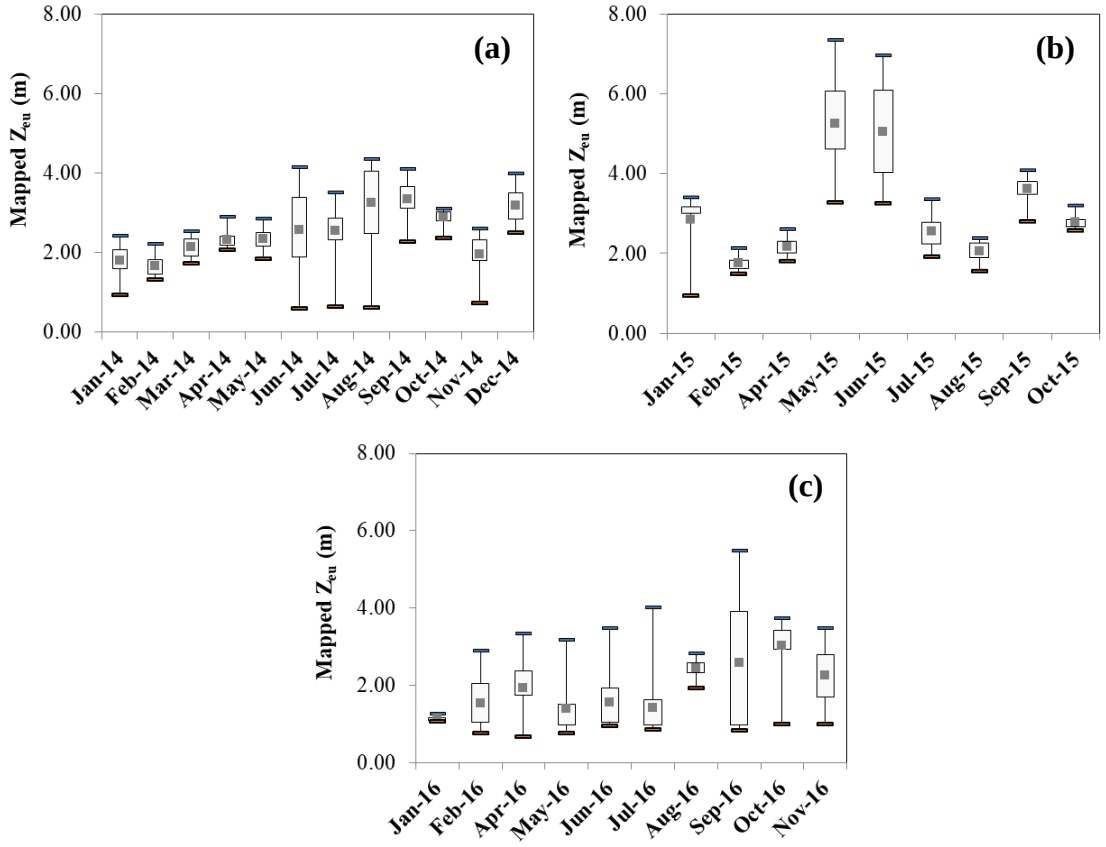

The drought event in Tietê River in 2014 reduced drastically the precipitation rate in Bariri (Figure 3.6), mainly in dry period; the Z_{eu} values were below of 4 m in most reservoir (Figure 3.8a). The high variability (from 0.59 to 4.34 m) was observed in August month with expressive decreasing of Z_{eu} in zone A, where it was verified an algal bloom episode in analysis of the respective satellite image. The variability reduced in February and October, with lowest Z_{eu} values in the former month (average of 1.65 m) in the beginning of drought, in relation to October (2.88 m). May-2014 showed a slight Z_{eu} variability (from 1.83 to 2.84 m), characterized by the stain aspect (Figure 3.7a).

The 2016 year presents the lowest Z_{eu} values for February, May and October in relation to previous years (Figure 3.8c). The Z_{eu} variability was lower in February with average of 1.54 m and in October with average of 3.00 m, when the Z_{eu} values remained closest to the maximum (Figure 3.8c). The wet period of 2016 presented great amount of rainfall with high precipitation rate in January (~ 300 mm) which possibly enriched the runoff process and, consequently, the increment of a great amount of suspended material into the reservoir, increasing turbidity and reducing Z_{eu} in February. In May-2016 (Z_{eu} average of 1.40 m), it was possible to see the Z_{eu} increase in some part of zone A and in zone B. In August-2016, the Z_{eu} average was 2.46 m with low variability (Figure 3.8c); it was compatible with the high [Chl-*a*] values (range from ~ 100 to 234 μg L^{-1}) found in BAR1 survey in the sample points in zone A, increasing the turbidity and reducing the Z_{eu} values. It was possible to see that Z_{eu} followed a pattern, with high values in months of dry periods, when the amount of rainfall is reduced. Tang *et al.* (2007), analyzing the annual variation of Z_{eu}, showed that in South China Sea, the values were lower in December-February (correspondent to austral summer) than in June-August (correspondent to austral winter).

3.3.7. Z_{SD} using satellite-derived data

The spatial distribution of Z_{SD} (Lee *et al.*, 2013) also consisted of years of 2014, 2015 and 2016 and the same months of Z_{eu} spatialization were highlighted (Figure 3.9); boxplot graphics (Figure 3.10) were also constructed to comprise the statistical performance of Z_{SD} model in Bariri reservoir. The maximum Z_{SD} value found was 2.95 m in May-15 and the minimum value was 0.32 m in June-2014, same months of minimum and maximum, respectively, in Z_{eu} spatialization (Figure 3.9a-b). The Z_{SD}

variability in May-15 was from 1.23 to 2.95 m and from 0.32 to 1.74 m in June-14 (Figure 3.10a-b). The zone A presented low Z_{SD} values with the exception of May-15, where Z_{SD} values were high and in zone B, the Z_{SD} was low in relation to the reservoir in upstream direction. The Z_{SD} in May-15 and June-15 showed highest values for these years (Figure 3.10b), accompanied by the atypical rainfall observed in this period. In 2014, the highest Z_{SD} was in August (varying from 0.33 to 1.87 m) with decrease in zone B due to an algal bloom episode which reduced the water transparency (Figure 3.9a).

Figure 3.9. Spatial distribution of Z_{SD} using the model from Lee *et al.* (2015) for February, May, August and October months of (a) 2014, (b) 2015 and (c) 2016. The A and B arrows highlight zones which presented high variability in Z_{SD} values among the images analyzed.

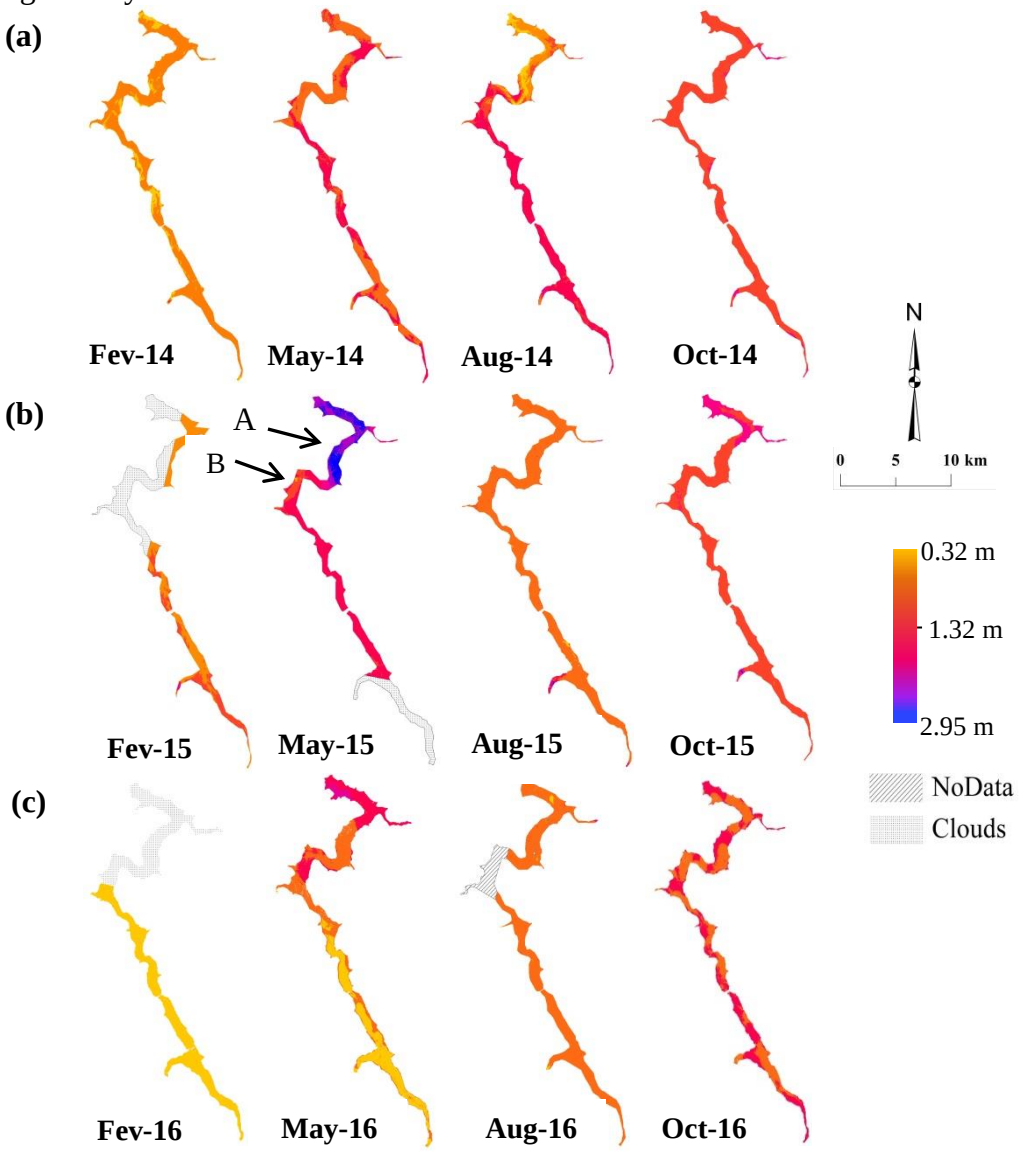

In May-14, the Z_{SD} was low (mean of 1.00 m), varying from 0.68 to 1.25 m. February and October months, in 2014, showed Z_{SD} means of 0.67 m and 0.93 m, respectively. In 2016, the high precipitation rate in January can be related to the Z_{SD} reduce in respective month and in February month, which showed the most values close to the minimum (1.25 m) according to the boxplot and the spatialization (Figures 3.9c, 3.10c). In May-16, the Z_{SD} values remained close to the minimum, varying from 1.14 m to 4.84 m, with the increase of Z_{SD} in zones A and B. In August-16, Z_{SD} varied from 0.54 to 0.88 m, showing low variability (Figure 3.10c). The Z_{SD} measured *in situ* in the same month, varied from 0.50 to 1.60 m. In October-16 image (Figure 3.9c); it was possible to observe visually the variability (0.67 to 1.17 m) of Z_{SD} when the values remained close to the maximum value (Figure 3.10c).

Figure 3.10. Boxplots of Z_{SD} spatial distributions in Bariri reservoir for 2014 (a), 2015 (b) and 2016 (c).

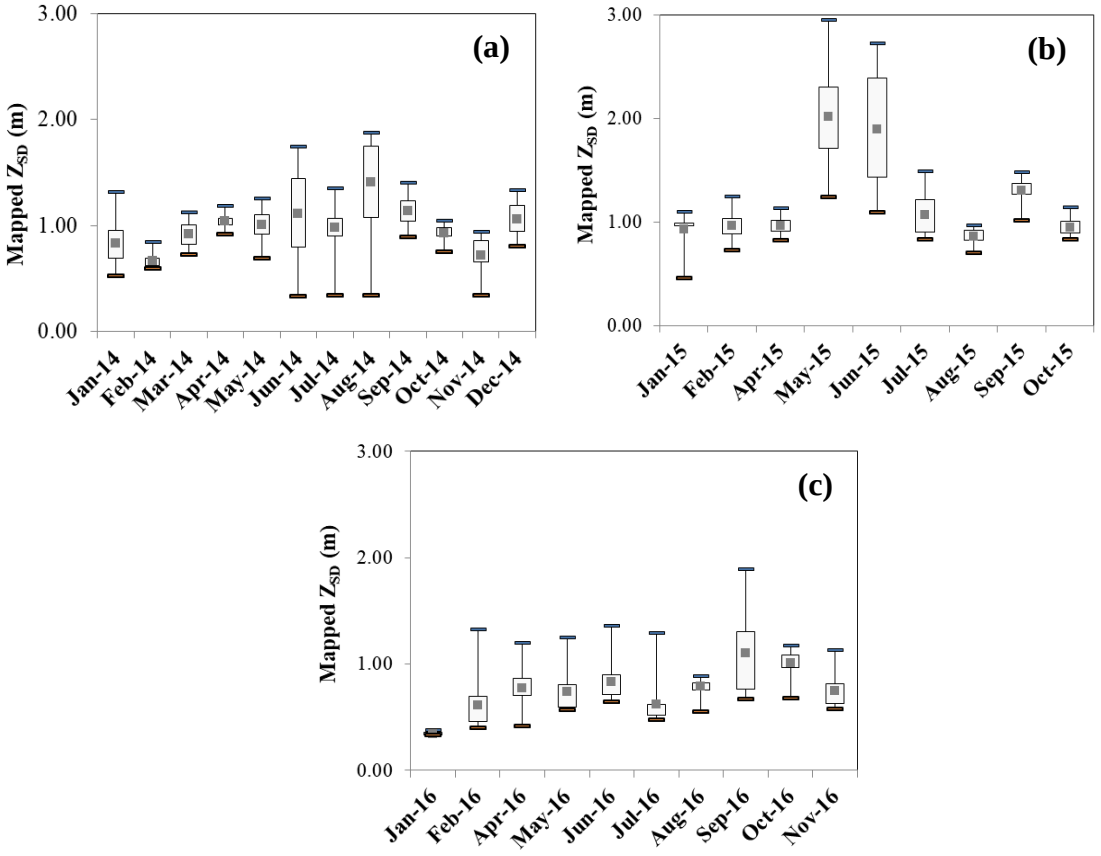

The patterns of Z_{eu} and Z_{SD} images were the same with different magnitudes, indicating that the Z_{SD} also is influenced by seasonal differences among the dry and wet periods and influence of external material in Bariri reservoir. In 2014, due to the occurrence of the drought event in Tietê River, it was not possible to delineate the effect

of seasonality in Z_{SD} values, however, it was observed that in months which achieved the lowest rainfall values (January, June and August, for instance) the Z_{SD} was the highest. In 2015, the months in the dry period (mainly, May and June) showed high Z_{SD} and, in 2016, the Z_{SD} increased according to reduce of rainfall in the dry period. Al Kaabi *et al.* (2016) registered that in Arabian Gulf, the Z_{SD} was higher in April-September period than in October-March period. Such seasonal variability was observed in Z_{SD} studies that the lowest values were found in summer and spring, when the rainfall is higher, in relation to winter (decrease of rainfall) that showed higher Z_{SD} (Wu *et al.*, 2015; Rodrigues *et al.*, 2017).

3.4. Discussion

3.4.1. Relationships between Z_{eu}; Z_{SD} and water quality constituents

In both field campaigns, the SPM concentration ([SPM]) was dominated by organic matter. The relationship between [SPM] and [Chl-*a*] was strong in BAR1 (R = 0.985; $p < 0.001$), however, in BAR2, the relationship was much weaker (R = 0.369) with no significance. The second field campaign had the [Chl-*a*] reduced and the organic matter in [SPM] was almost totally dominated by $a_{CDOM}(443)$ with the correlation of R = 0.996 ($p < 0.001$) while the relationship with $a_{phy}(443)$ was not significant. When the data of the two field campaigns were aggregated, the relationship between [SPM] and [Chl-*a*] (R = 0.984; $p < 0.001$) was very close of the relationship of BAR1.

The Z_{eu} models tested in this study and, mainly, the Z_{eu}_Zhao used for mapping the euphotic zone in Bariri reservoir showed increasing of the errors when applied for BAR2 (RMSD = 0.88 m; ε = 19.66%; *bias* = - 0.38 m) in relation to BAR1 (RMSD = 0.46; ε = 15.12%; *bias* = - 0.38 m). The relationship between Z_{eu} and [SPM] in BAR2 was extremely weak (R = 0.10) and it is due to the high correlation of $a_{CDOM}(443)$ with [SPM] once the relationship between Z_{eu} and [SPM] was higher for BAR1 than for the aggregated data (R = 0.62 and R = 0.56, respectively). The errors of Z_{eu} estimations when applied for all dataset had a slight increase in relation to BAR1 (RMSD = 0.64 m; ε = 16.76%; *bias* = - 0.33 m). Therefore, the predominance of a_{CDOM} and the decreasing of [Chl-*a*] in BAR2 increased the mismatch between Z_{eu}_Zhao estimations and *in situ* Z_{eu}.

Figure 3.11 shows that the Z_{eu} is negatively correlated to [SPM] (R = - 0.546; $p < 0.001$), [Chl-*a*] (R = - 0.557; $p < 0.001$) and turbidity (R = - 0.550; $p < 0.001$). So, the Z_{eu} measured *in situ* was slightly affected by [Chl-*a*] in the Bariri all dataset. The correlation between [SPM] and $a_{phy}(443)$ found in Bariri all dataset confirms the predominance of organic matter in the optical environment (R = 0.836; $p < 0.001$). High values of [Chl-*a*] indicates excessive input of nutrients in water; these regions present deficit in underwater light and, therefore, reduction of euphotic depths (Liu *et al.*, 2016). The nutrients enrichment in water, accelerate the primary productive with great amount of phytoplankton production which was verified trough the strong relationship between [Chl-*a*] and $a_{phy}(443)$ which was R = 0.885; $p < 0.001$ (Figure 3.11). The correlation between [Chl-*a*] was not significant (not shown here).

Figure 3.11. Relationships between *in situ* Z_{eu} and (a) [Chl-*a*], (b) [SPM], (c) turbidity and between the $a_{phy}(443)$ with (d) [SPM] and (e) [Chl-*a*].

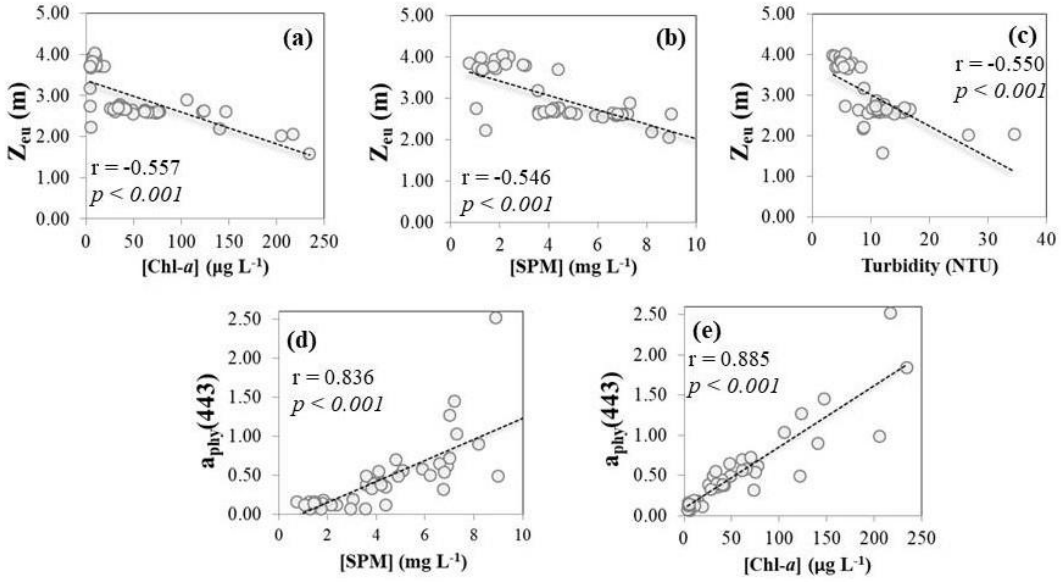

The high [Chl-*a*] verified in BAR1 and predominance of a_{CDOM} in the total absorption of light in both field campaigns suggest a multiple external sources of organic matter entrance in Bariri reservoir depicted by the meteorological conditions, urban/industrial and agricultural waste. In addition, no significant correlation between [Chl-*a*] and a_{CDOM} was verified in neither of the two field campaigns that cannot confirm the influence of autochthonous CDOM in Bariri reservoir system (Binding *et al.*, 2008). Alterations in land use and land cover (LULC) in sub-watershed of Barra Bonita reservoir (upstream of Bariri reservoir) showed replacement of forest fragments by grazing land advanced and intensification of sugarcane production, promoting

erosion, soil degradation and, consequently, reducing of water quality (Gomes *et al.*, 2017a).

In relation to Z_{SD}, the semi-analytical model to estimate water transparency from Lee *et al.* (2013) also showed an expressive increase of mismatching between the estimations and Z_{SD} measured when applied for BAR2 in relation to BAR1. The errors increased around 63% in the first field campaign in relation to the second with RMSD = 0.41; ε = 34.10%; *bias* = - 0.18 m in BAR1 and RMSD = 1.39; ε = 97.70%; *bias* = - 1.30 m in BAR2; the underestimations were observed in all sample points.

In BAR1, inverse correlations were verified: Z_{SD} and [Chl-*a*] (R = - 0.737; $p < 0.001$); Z_{SD} and [SPM] (R = -0.786; $p < 0.001$); Z_{SD} and turbidity (R = - 0.652; $p < 0.001$). However, in BAR2, no correlation was verified between Z_{SD} and the OSS; the relationship between Z_{SD} and turbidity was also inverted (R = - 0.695; $p < 0.05$). The BAR2 survey showed [Chl-*a*] mean of 7.99 ± 4.10 μg L^{-1} whereas in BAR1 survey, the mean was 119.76 ± 96.43 μg L^{-1}; the absorption of light in both field campaigns was dominated by CDOM. The Z_{SD} is a reasonable indicator of trophic conditions once it was inversely correlated to [Chl-*a*], however it was not observed in colored lakes with low [Chl-*a*] (Gholizadeh *et al.*, 2016), justified by the high mismatch of Z_{SD} estimations in BAR2 related to *in situ* Z_{SD}.

Considering the Bariri all dataset, the relationships between *in situ* Z_{SD} and [Chl-*a*], [SPM] and turbidity were inverses (R = - 0.658; $p < 0.001$, R = - 0.655; $p < 0.001$ and R = - 0.643; $p < 0.001$, respectively) (Figure 3.12).

Figure 3.12. Relationships between *in situ* Z_{SD} and (a) [Chl-*a*], (b) [SPM], (c) turbidity.

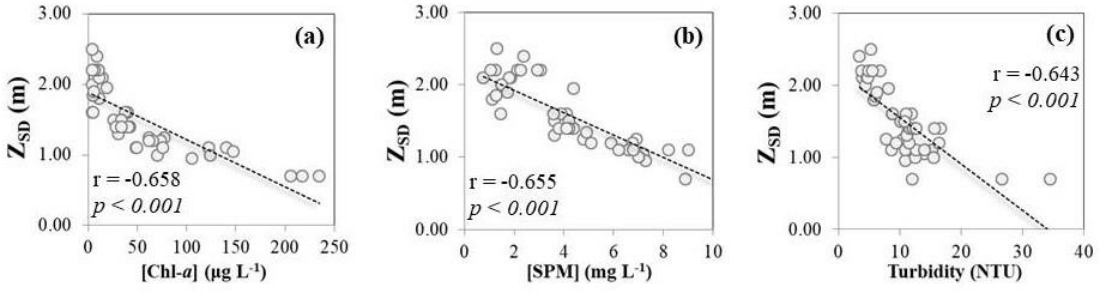

The Z_{SD} varied inversely in relation to OSS concentrations and turbidity; sampling points with high [Chl-*a*] and [SPM], and, consequently high turbidity values, presented low Z_{SD}; the effect of phytoplankton production on water transparency was identified by the reduction of Z_{SD}. The *in situ* Z_{eu} and Z_{SD} showed similar responses to influence of

optical constituents in Bariri reservoir, with Z_{SD} showing highest correlation with them. The relationship between the two parameters of water transparency and quality was significantly strong (R = 0.893; $p < 0.001$).

3.5. Conclusions

After the application of several tests with the Z_{eu} estimation models available for a wide range of waters, it was verified that the empirical model of Zhao *et al.* (2013) ($\varepsilon \sim$ 16.76%) excelled the semi-analytical algorithm performance presenting ($\varepsilon \sim$ 35.11%), countering the affirmation that IOP-centered approach is able to be applied in a wide range of bio-optical waters. The Z_{eu} semi-analytical algorithm achieved the lowest accuracy between all the others empirical models tested with the exception of the Z_{eu}_Wang ($\varepsilon \sim$ 37.91%).

The Z_{SD} estimations from the semi-analytical model presented uncertainties ($\varepsilon \sim$ 57%); the estimations were highly affected by the predominance of CDOM in Bariri reservoir ($\varepsilon \sim$ 97.7% when applied for BAR2) confirmed by the inexistence of correlation between Z_{SD} and [Chl-*a*] and Z_{SD} and [SPM], despite the reduction of the correlation between Z_{SD} and the OSS when the data was aggregated. The accuracies of Z_{eu} estimations among the tested models also compromised the results with the reduction of [Chl-*a*] in BAR2, however the magnitude was lesser than the Z_{SD} estimations once the correlation between Z_{eu} and [SPM] was higher in BAR2. It is possible to conclude that Z_{SD} is highly affected by the increase of [Chl-*a*].

The Z_{eu} *in situ* varied from 1.58 m to 4.00 m and Z_{SD} varied from 0.5 m to 2.50 m, showing reliable results of water transparency. The accuracy of Z_{SD} reading is subject to properties of observer eye as a contrast sensor; the boat shadow and also depends on the wind speed with an error varying from 0.2 to 0.5m (Alikas & Kratzer, 2017) whereas the Z_{eu} was obtained from $E_{d(PAR)}$ normalized to reduce the changes in sun illumination condition and in a geometry configuration to avoid the wind and boat shadow effects in radiometric data acquisition.

Using the atmospherically corrected OLI/Landsat-8 (LaSRC) Z_{eu} and Z_{SD} images, we verified the seasonality pattern controlled by the rainfall in Z_{eu} and Z_{SD} which remained the same delineation but with different magnitudes. The Z_{eu} and Z_{SD} showed high values in the dry period (April-September); in contrast, showed low values in the

wet period (October-March), when the input of external material is facilitated in reservoir.

CHAPTER 4: Final Considerations

4.1. Highlights

The results achieved in this dissertation confirm the hypothesis that the semi-analytical algorithm (Lee *et al.*, 2013) to estimate k_d produced the lower errors (MAPE = 41.04% and RMSD = 1.07 m^{-1}) among others semi-analytical and empirical models; the k_d semi-analytical model was effective to map the attenuation coefficient and to be an intermediary product for Z_{eu} and Z_{SD} estimations. In a semi-analytical scheme, the Z_{SD} was derived as an inverse relation with k_d through the semi-analytical model from Lee *et al.* (2015). The accuracy achieved in Z_{SD} estimations was lesser than the k_d estimations through the semi-analytical scheme (ε = 57.10% and RMSD = 0.90 m) and it was related to the strong influence of CDOM in the Z_{SD}.

The Z_{eu} and Z_{SD} estimations were affected by the CDOM dominance in Bariri reservoir and the accuracies of estimations were more compromise in BAR2 where the influence of CDOM was higher than in BAR1. The Z_{eu} and Z_{SD} are highly related to precipitation, presenting the highest values in dry periods, where the input of external material is reduced.

The applicability of the semi-analytical equation to estimate Z_{eu} developed by Lee *et al.* (2007) was not verified with high errors (ε = 35.11% and RMSD = 1.40 m) in relation to the empirical model by Zhao *et al.* (2013) (ε = 16.76% and RMSD = 0.64 m). These results suggest that the Z_{eu} was more represented by a model developed for an aquatic environmental with similar optical constituents to Bariri reservoir than for a semi-analytical model using the IOP approach and calibrated for waters optically described only by phytoplankton.

From the spatialization, the inverse relation between k_d; Z_{eu} and k_d; Z_{SD} was observed, with the high k_d values correspondent to low Z_{eu} and Z_{SD} values where the increase of the attenuation of light indicates increase of water constituents and, consequently, increase of turbidity and reduce of the Z_{eu} and Z_{SD}.

To our knowledge, there is no previous study to assess the potentiality of Landsat-8/OLI data to estimate and map the water clarity parameters considered in this research in inland waters dominated by CDOM. The QAA_v5 in the configuration of the band centers of the Landsat-8/OLI was able to estimate the IOPs used in the semi-analytical

model to derive k_d, making possible the estimations of Z_{eu} and Z_{SD} and the asses of the temporal-spatial distribution of the water clarity parameters in Bariri reservoir.

REFERENCES

Alcântara, E.; Novo, E.; Stech, J.; Lorenzzetti, J.; Barbosa, C.; Assireu, A.; Souza, A. (2010) A contribution to understanding the turbidity behaviour in na Amazon flooplain. Hydrology and Earth System Sciences. v. 14. p. 351-364.

Alcântara, E.; Bernardo, N.; Watanabe, F.; Rodrigues, T.; Rotta, L.; Carmo, A.; Shimabukuro, M.; Gonçalvez, S.; Imai, N. (2016) Estimating CDOM absorption coefficient in tropical inland waters using OLI/landsat-8 images. Remote Sensing Letters. v. 7. p. 661-670.

Alikas, K.; Kratzer, S. (2017) Improved retrieval of Secchi depth for optically-complex waters using remote sensing data. Ecological Indicators. v. 77. p. 218-277.

Al Kaabi, M. R.; Zhao, J.; Ghedira, H. (2016) MODIS-Based Mapping of Secchi Disk Depth Using a Qualitative Algorithm in the Shallow Arabian Gulf. Remote Sensing. v. 8. p. 1-17.

APHA. AMERICAN PUBLIC HEALTH ASSOCIATION. (1998) Standard methods for the examination of water and wastewater.

Austin, R. W.; Petzold, T. (1981) The determination of the diffuse attenuation coefficient of sea water using the Coastal Zone Color Scanner. In Oceanography from Space. Plenum Press. p. 239-256.

Barbosa, F. A. R.; Padisák, J.; Espíndola, E. L. G.; Borics, G.; Rocha, O. (1999) The cascading reservoir continuum concept (CRCC) and its application to the river Tietê-basin, São Paulo State, Brazil. In Workshop on Theoretical Reservoir Ecology and its Applications. p. 425-437.

Barsi, J. A.; Lee, K.; Kvaran, G.; Markham, B. L. Pedelty, J. A. (2014) The spectral response of the Landsat-8 Operational Land Imager. Remote Sensing of Environment. v. 6. p. 10232-10251.

Bernardo, N.; Watanabe, F.; Rodrigues, T.; Alcântara, E. (2016) Evaluation of the suitability of MODIS, OLCI and OLI for mapping the distribution of total suspended matter in the Barra Bonita Reservoir (Tietê River, Brazil). Remote Sensing Applications: Society and Environment. v. 4. p. 68-82.

Bernardo, N.; Watanabe, F.; Rodrigues, T. Alcântara, E. (2017) Atmospheric correction issues for retrieving total suspended matter concentrations in inland waters using OLI/Landsat-8 image. Advances in Space Research. v. 59. p. 2335-2348.

Binding, C. E.; Jerome, J. H.; Bukata, R. P.; Booty, W. G. (2008) Spectral absorption properties of dissolved and particulate matter in Lake Erie. Remote Sensing of Environment. v. 112. p. 1702-1711.

Brezonik, P. L.; Olmanson, L. G.; Finlay, J. C.; Bauer, M. E. (2015) Factor affecting the measurement of CDOM by remote sensing of optically complex inland waters. Remote Sensing of Environment. v. 157. p. 199-215.

Bricaud, A.; Morel, A.; Prieur, L. (1981) Absorption by dissolved organic matter of the sea (yellow substance) in the UV and visible domains. Limnology and Oceanography. v. 26. p. 43-53.

Bukata, R. P.; Jerome, J. H.; Kondratyev, K. Y.; Pozdnyakov, D. V. (1995) Optical Properties and Remote Sensing of Inland and Coastal Waters. Florida: CRC Press.

Cairo, C. T.; Barbosa, C. C. F.; Novo, E. M. L. M.; Calijuri, M. C. (2017) Spatial and seasonal variation in diffuse attenuation coefficients of downward irradiance at Ibitinga Reservoir, São Paulo, Brazil. Hydrobiologia. v. 784. p. 265-282.

Calijuri, M. C.; Dos Santos, A. C. A.; Jati, S. (2002) Temporal changes in the phytoplankton community structure in a tropical and eutrophic reservoir (Barra Bonita, S.P. – Brazil). Journal of Plankton Research. v. 24. p. 617 – 634.

Chauhan, P.; Sahay, A.; Rajawat, A. S.; Nayak, S. (2003) Remote sensing of diffuse attenuation coefficient *(K490)* using IRS-P4 Ocean Colour Monitor (OCM) sensor. Indian Journal of Marine Sciences. v. 32. p. 279-284.

Coelho, C. A. S.; Cardoso, D. H. F.; Firpo, M. A. F. (2015) Precipitation diagnostics of an exceptionally dry event in São Paulo, Brazil. Theoretical and Applied Climatology. v. 125. p. 769-784.

Concha, J., Schott, J. (2016) Retrieval of color producing agents in case 2 waters using Landsat 8. Remote Sensing of Environment. v. 185. p. 95–107.

Gallegos, C. L.; Correll, D. L.; Pierce, J. W. (1990) Modeling spectral diffuse attenuation, absorption, and scattering coefficients in a turbid estuary. Limnology and Oceanography. v. 35. p. 1486-1502.

Gitelson, A. A.; Schallles, J. F.; Hladik, C. M. (2007) Remote chlorophyll-*a* retrieval in turbid, productive estuaries: Chesapeake Bay case study. Remote Sensing of Environment. v. 109. p. 464-472.

Gholizadeh, M. H.; Melesse, A. M.; Reddi, L. (2016) A comprehensive review on water quality parameters estimation using remote sensing techniques. Sensors. v. 16. 1-43.

Golterman, H. L.; Clymo, R. S.; Ohnstad, M. A. M. (1978) Methods for physical and chemical analysis of fresh water. Blackwell Scientific Publications, Oxford.

Gomes, A. C. C.; Bernardo, N. M. R.; Alcântara, E. (2017) Accessing vegetation health in a drought and land use and land cover changing scenario. Natural Hazards. v. 89. p. 1401-1420.

Kratzer, S. Brockmann, C.; Moore, G. (2008) Using MERIS full resolution data to monitor coastal waters - A case study from Himmerfjärden, a fjord-like bay in the northwertern Baltic Sea. Remote Sensing of Environment. v. 112. p. 2284-2300.

Kirk, J. T. O. Light & Photosynthesis in Aquatic Ecosystems. 2nd Edition. (1994) Melbourne: Cambridge University Press.

Le, C. F.; Li, Y. M.; Zha, Y.; Sun, D.;Yin, B. (2009) Validation of a Quasi-Analytical Algorithm for highly turbid eutrophic water of Meiliang Bay in Taihu Lake, China. IEEE Transactions on Geoscience and Remote Sensing. v. 47. p. 2492-2500.

Lee, Z.P., Carder, K.L., Arnone, R.A. (2002) Deriving inherent optical properties from water color: a multiband quasi-analytical algorithm for optically deep waters. Applied Optics. v. 41. p. 5755–5772.

Lee, Z. P.; Du, K. P.; Arnone. (2005) A model for the diffuse attenuation coefficient of downwelling irradiance. Journal of Geophysical Research. v. 110. p. 1-10.

Lee, Z.P.; Weidemann, A.; Kindle, J.; Arnone, R.; Carder, K. L.; Davis, Curtiss. (2007) Euphotic zone depth: Its derivation and implication to ocean-color remote sensing. Journal of Geophysical Research. v. 112. p. 1-11.

Lee, Z.P., Lubac, B., Werdell, J., Arnone, R. (2009) An Update of the Quasi-analytical Algorithm (QAA_v5). IOCCG.

Lee, Z. P.; Ahn, Y. H.; Mobley, C.; Arnone, R. (2010) Removal of surface-reflected light for the measurement of remote-sensing reflectance from an above-surface platform. Optics Express. v. 18. p. 26313-26324.

Lee, Z. P; Hu, C.; Shang, S.; Du, K.; Lewis, M.; Arnone, R.; Brewin, R. (2013) Penetration of UV-visible solar radiation in the global oceans: insights from ocean color remote sensing. Journal of Geophysical Research: Oceans. v. 118. p. 4241-4255.

Lee, Z. P.; Shang, S.; Hu, C.; Du, K.; Weidemann, A.; Hou, W.; Lin, J.; Lin, G. (2015) Secchi disk depth: A new theory and mechanistic model for underwater visibility. Remote Sensing of Environment. v. 169. p. 139-149.

Lee, Z.P.; Shang, S.; Qi, L.; Yan, J.; Lin, G. (2016) A semi-analytical scheme to estimate Secchi-disk depth from Landsat-8 measurements. Remote Sensing of Environment. v. 177. p. 101-106.

Lee, Z.P.; Shang, S.; Stavn, R. (2018) AOPs are not additive: on the biogeo-optical modeling of the diffuse attenuation coefficient. Frontiers in Marine Science. v. 5. p. 1-5.

Li, S.; Song, K.; Mu, G.; Zhao, Y.; Ma, J.; Ren, J. (2016) Evaluation of the Quasi-Analytical Algorithm (QAA) for estimating total absorption coefficient of turbid inland Waters in Northeast China. IEEE Journal of Selected Topics in App. Earth Observations and Remote Sensing. v. 9. p. 1939-1404.

Lira, G. A. S. T.; Oliveira, M. C. B.; Moura, A. N. (2009) Structure and dynamics of phytoplankton community in the Botafogo reservoir-Pernambuco-Brazil. Brazilian Archives of Biology and Technology. v. 52. p. 493-501.

Liu, X.; Zhang, Y.; Shi, K.; Lin, J.; Zhou, Y. (2016) Determining critical light and hydrologic conditions for macrophyte presence in a large shallow lake: The ratio of euphotic depth to water depth. Ecological Indicators. v. 71. p. 317-326.

Ma, J.; Song, K.; Wen, Z.; Zhao, Y.; Shang, Y.; Fang, C.; Du, Jia. (2016) Spatial Distribution of Diffuse Attenuation of Photosynthetic Active Radiation and Its Main Regulating Factors in Inland Waters of Northeast China. Remote Sensing. v. 964. p. 1-17.

Majozi, N. P.; Salama, M. S.; Bernard, S.; Harper, D. M.; Habte, M. G. (2014) Remote sensing of euphotic depth in shallow tropical inland waters of Lake Naivasha using MERIS data. Remote Sensing of Environment. v. 148. p. 178-189.

Mishra, D. R.; Narumalani, S.; Rundquist, D.; Lawson, M. (2005) Characterizing the vertical diffuse attenuation coefficient for downwelling irradiance in coastal waters: Implications for water penetration by high resolution satellite data. ISPRS Journal of Photogrammetry and Remote Sensing. v. 60. p. 48-64.

Mishra, S.; Mishra, D. R.; Lee, Z. P.(2014) Bio-optical inversion in highly turbid and cyanobacteria-dominated waters. IEEE Transactions on Geoscience and Remote Sensing. v. 52. p. 375 – 388.

Mobley, C.D. (1994) Light and water: radiative transfer in natural waters. San Diego, CA, USA: Academic Press.

Mobley, C. D. (1999) Estimation of the remote-sensing reflectance from above-surface measurements. Applied Optics. v. 38. p. 7442-7455.

Morel, A., (1988) Optical modeling of the upper ocean in relation to its biogenous matter content (case I waters). Journal of Geophysical Research. v. 93. p. 749–710.

Morel, A.; Huot, Y.; Gentili, B.; Werdell, P. J.; Hooker, S. B. Franz, B. A. (2007) Examining the consistency of products derived from various ocean color sensors in open ocean (Case 1) waters in the perspective of a multi-sensor approach. Remote Sensing of Environment. v. 111. p. 69-88.

Moses, W. J.; Gitelson, A. A.; Perk, R. L.; Gurlin, D.; Rundquist, D. C.; Leavitt, B. C.; Barrow, T. M.; Brakhage, P. (2012) Estimation of chlorophyll-*a* in turbid productive waters using airborne hyperspectral data. Water Research. v. 46. p. 993-1004.

Mueller, J. L.; Trees, C. C. (1997) Revised SeaWiFS prelaunch algorithm for diffuse attenuation coefficient K(490), NASA Technical Memorandum, TM-104566. Greenbelt, Md: NASA Goddard Space Flight Center. v. 41. p. 18-21.

Mueller, J. L. (2000). SeaWiFS algorithm for the diffuse attenuation coefficient, $K_d(490)$ using water-leaving radiance at 490 and 555 nm. In SeaWiFS post launch technical report series, part 3. S. B. Hooker. v. 11. p. 24−27.

NASA (2015). Drought Shrinking São Paulo Reservoirs. Available on: http://earthobservatory.nasa.gov/NaturalHazards/view.php?id=84564&eocn=image&eoci=morenh. Accessed February 2017.

Olmanson, L. G.; Bauer, M. E.; Brezonik, P. L. (2008) A 20-year Landsat water clarity census of Minnesota's 10,000 lakes. Remote Sensing of Environment. v. 112. p. 4086-4097.

Olmanson, L. G.; Brezonik, P. L.; Finlay, J. C.; Bauer, M. E. (2016) Comparison of Landsat 8 and Landsat 7 for regional measurements of CDOM and water clarity in lakes. Remote Sensing of Environment. v. 185. p. 119-128.

Pahlevan, N,; Schott, J. R.; Franz, B. A.; Zibordi, G.; Markham, B.; Bailey, S.; Schaaf, C. B.; Ondrusek, M.; Greb, S.; Strait, C. M. (2017) Landsat 8 remote sensing reflectance (R_{rs}) products: Evaluations, intercomparisons, and enhancements. Remote Sensing of Environment. v. 190. p. 289-301.

Pamplin, P. A. Z. (2004) Estudo comparativo da estrutura da comunidade bentônica de duas represas com diferenças no grau de eutrofização. Tese (Doutorado em Ciências).

Programa de Pós-Graduação em Ecologia e Recursos Naturais. Universidade Estadual de São Carlos. São Carlos. 125 p.

Prado, R. B.; Novo, E. M. L. M.; Pereira, M. N. (2007) Evaluation of Land Use and Land Cover Dynamics in the Hydrographic Contribution Basin of Barra Bonita Reservoir-SP. Revista Brasileira de Cartografia. v. 2. p. 127-135.

Preisendorfer, R.W. (1986). Secchi disk science: Visual optics of natural waters. Limnology and Oceanography. v. 31. p. 909–926.

Rodrigues, T. W. P.; Guimarães, U. S.; Rotta, L. H. S.; Watanabe, F. S. Y.; Alcântara, E.; Imai, N. N. (2016) Delineamento amostral em reservatórios utilizando imagens Landsat-8/OLI: Um estudo de caso no reservatório de Nova Avanhadava (estado de São Paulo, Brasil). BCG – Boletim de Ciências Geodésicas. v. 22. p. 303-323.

Rodrigues, T.; Alcântara, E; Watanabe, F.; Imai, N. (2017) Retrieval of Secchi disk depth from a reservoir using a semi-analytical scheme. Rem. Sens. of Environment. v. 198. p. 213-228.

Rotta, L. H. S.; Mishra, D. R.; Alcântara, E. H.; Imai, N. N. (2016) Analyzing the status of submerged aquatic vegetation using novel optical parameters. International Journal of Remote Sensing. v. 37. p. 3786-3810.

Tassan, S.; Ferrari, G. M. (1995) An alternative approach to absorption measurements of aquatic particles retained on filters. Limnology and Oceanography. v. 40. p. 1358-1368.

Tassan, S.; Ferrari, G. M. (1998) Measurement of light absorption by aquatic particles retained on filters: determination of the optical path length amplification by the ‘transmittance-reflectance’ method. Journal of Plankton Research. v. 20. p. 1699-1709.

Tassan, S.; Ferrari, G. M. (2002) A sensitivity analysis of the ‘Transmittance–Reflectance’ method for measuring light absorption by aquatic particles. Journal of Plankton Research. v. 24. p. 757-774.

Tundisi, J. G.; Matsumura-Tundisi, T.; Pareschi, D. C.; Luzia, A. P.; Von Haeling, P. H.; Frollini, E. H. (2008) A bacia hidrográfica do Tietê/Jacaré: estudo de caso em pesquisa e gerenciamento. Estudos Avançados. v. 22. p. 159-172.

USGS. U. S. Geological Survey (2018) Product Guide. Landsat 8 Surface Reflectance Code (LASRC) Product. Department of the Interior. Version 4.3.

Shang, S.; Lee. Z.; Shi. L.; Lin, G.; Wei, G.; Li, X. (2016) Changes in water clarity of the Bohai Sea: Observations from MODIS. Remote Sensing of Environment. v. 186. p. 22-31.

Vermote, E., Justice, C., Claverie, M., Franch, B. (2016) Preliminary analysis of the performance of the Landsat 8/OLI land surface reflectance product. Remote Sensing of Environment. v. 185. p. 46–56.

Wang, M.; Son, S.; Harding Jr., L. W. (2009) Retrieval of diffuse attenuation coefficient in the Chesapeake Bay and turbid ocean regions for satellite ocean color applications. Journal of Geophysical Research. v. 114. p. 1-15.

Watanabe, F. S. Y.; Alcântara, E. Rodrigues, T. W. P.; Imai, N. N.; Barbosa, C. C. F.; Rotta, L. H. S. (2015) Estimation of Chlorophyll-*a* Concentration and the Trophic State of the Barra Bonita Hydroelectric Reservoir Using OLI/Landsat-8 Images. International Journal of Environmental Research and Public Health. v. 12. p. 10391-10417.

Watanabe, F.; Mishra, D. R.; Astuti, I.; Rodrigues, T.; Alcântara, E.; Imai, N. N.; Barbosa, C. (2016) Parametrization and calibration of a quase-analytical algorithm for tropical eutrophic waters. ISPRS Journal of Photogrammetry and Remote Sensing. v. 121. p. 28-47.

Wetzel, R. G. Limnology: Lake and river ecosystems. 3rd Edition. (2001) Elsevier Academic Press.

Wu, Z.; Zhang, Y.; Zhou, Y.; Liu, M.; Shi, K.; Yu, Z. (2015) Seasonal-Spatial distribution and long-term variation of transparency in Xin'anjiang reservoir: implications for reservoir management. International Journal of Environmental Research and Public Health. v. 12. p. 9492-9507.

Yang, W.; Matsushita, B.; Chen, J.; Yoshimura, K.; Fukushima, T. (2013) Retrieval of inherent optical properties for turbid inland waters from remote-sensing reflectance. IEEE Transactions on Geoscience and Remote Sensing. v. 51. p. 3761-3773.

Yang, W.; Matsushita, B.; Yoshimura, K.; Chen, J.; Fukushima, T. (2015) A modified semianalytical algorithm for remotely estimating euphotic zone depth in turbid inland waters. IEEE Journal of Selected Topics in Applied Earth Observations and Remote Sensing. v. 8. p. 1545-1554.

Zhao, J.; Barnes, B.; Melo, N.; English, D.; Lapointe, B.; Muller-Karger, F.; Schaeffer, B.; Hu, C. (2013) Assessment of satellite-derived diffuse attenuation coefficients and euphotic depths in south Florida coastal waters. Remote Sensing of Environment. v. 131. p. 35-50.

Zhang, Y.; Dijk, M.; Liu, M.; Zhu, G.; Qin, B. (2009) The contribution of phytoplankton degradation to chromophoric dissolved organic matter (CDOM) in eutrophic shallow waters lakes: Field and experimental evidence. Water Research. v. 43. P. 4685-4697.

Zhang, Y.; Liu, X.; Yin, Y.; Wang, M.; Qin, B. (2012) A simple optical model to estimate diffuse attenuation coefficient of photosynthetically active radiation in an extremely turbid lake from surface reflectance. Optics Express. v. 20. p. 20482-20493.

Zheng, Z.; Ren, J.; Li, Y.; Huang, C.; Liu, G.; Du, C.; Lyu, H. (2016) Remote sensing of diffuse attenuation coefficient patterns from Landsat 8 OLI imagery of turbid inland waters: A case study of Dongting Lake. Science of the Total Environment. v. 573. p. 39-54.

Zhu, W.; Yu, Q.; Tian, Y. Q.; Becker, B. L.; Zheng, T.; Carrick, H. J. (2014) An assessment of remote sensing algorithms for colored dissolved organic matter in

complex freshwaters environments. Remote Sensing of Environment. v. 140. p. 766-778.